

Raman mapping of photodissociation regions in the Orion Nebula

William J. Henney*

Instituto de Radioastronomía y Astrofísica, Universidad Nacional Autónoma de México, Apartado Postal 3-72, 58090 Morelia, Michoacán, Mexico

Accepted XXX. Received YYY; in original form ZZZ

ABSTRACT

I show that the broad Raman-scattered wings of H α can be used to map neutral gas illuminated by high-mass stars in star forming regions. The near wings ($\Delta\lambda \approx \pm 10 \text{ \AA}$) trace neutral hydrogen columns of about $5 \times 10^{20} \text{ cm}^{-2}$, while the farther wings ($|\Delta\lambda| > 30 \text{ \AA}$) trace columns of about $5 \times 10^{21} \text{ cm}^{-2}$. Absorption features in the pseudo-continuum at 6633 and 6664 \AA correspond to neutral oxygen far-ultraviolet absorption lines at 1027.43 \AA and 1028.16 \AA . I apply this technique

Key words: Atomic physics – Radiative transfer – Photodissociation regions

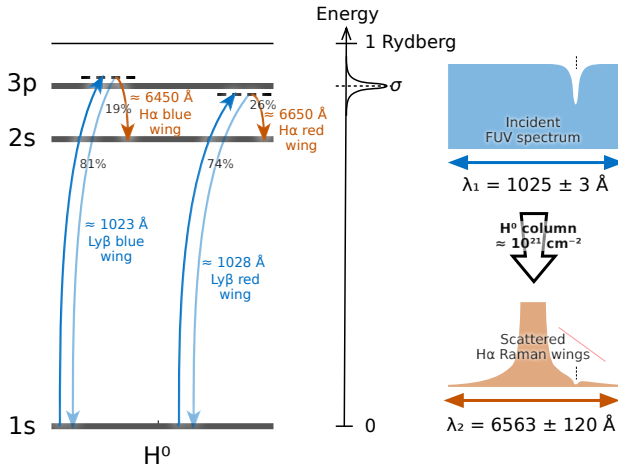


Figure 1. Schematic illustration of Raman scattering of photons from the Ly β wings to the H α wings. The relevant energy levels of neutral hydrogen are shown at left. Far ultraviolet photons that are shifted by about $\Delta\lambda_1 = \pm 1$ to 3 \AA from the Ly β rest wavelength can excite transitions from the ground 1s level to a virtual state adjacent to 3p. Most such excitations decay back to 1s (Rayleigh scattering), but in about one-fifth of cases the decay is to 2s instead (Raman scattering). The scattering cross section falls approximately as $\Delta\lambda_1^{-2}$, which gives broad Lorentzian wings to the H α line, as shown at right. A bandwidth of $\Delta\lambda_1 = \pm 3 \text{ \AA}$ around Ly β is transformed to a bandwidth $\Delta\lambda_2 \approx \pm 120 \text{ \AA}$ around H α . A narrow absorption line in the incident FUV spectrum (vertical thin dashed line) becomes a much broader notch in the scattered wings.

1 INTRODUCTION

Raman scattering is the inelastic analog of Rayleigh scattering by atoms or molecules. Both processes begin with a radiation-induced

transition of an electron to a virtual bound state (non-eigenstate). In Rayleigh scattering, the electron returns to its original state, resulting in the radiation being re-emitted with its original frequency (elastic scattering). In Raman scattering, on the other hand, the electron undergoes a transition to a different excited state, resulting in radiation being re-emitted at a much lower frequency. See Figure 1 for an illustration of the process. Recently, Dopita et al. (2016) identified exceedingly broad wings to the H α 6563 \AA line in the Orion Nebula and a number of H II regions in the Magellanic Clouds, which they ascribe to Raman scattering of ultraviolet radiation in the vicinity of the Ly β 1025 \AA transition. Raman scattering in astrophysical sources was first identified in symbiotic stars (Schmid 1989), where FUV O VI emission lines at 1032 and 1038 \AA produce broad emission features at 6827 and 7088 \AA . This illustrates a curious feature of Raman scattering (Nussbaumer et al. 1989): the relative width $\Delta\lambda/\lambda$ of spectral features is amplified by a factor $\lambda(\text{H}\alpha)/\lambda(\text{Ly}\beta) \approx 6.4$ when passing from the FUV to the optical domain.

Dopita et al. (2016) propose that the Raman wings form at the transition zone near the ionization fronts in H II regions. However, the total neutral hydrogen column through the ionization front can be no more than about $10/\sigma_0 \approx 2 \times 10^{18} \text{ cm}^{-2}$, where $\sigma_0 \approx 6.3 \times 10^{-18} \text{ cm}^2$ is the ground-state hydrogen photoionization cross section at threshold (Osterbrock & Ferland 2006). The Raman scattering cross section at wavelengths responsible for the observed wings is much lower than this: $\sigma_{\text{Raman}} \sim 10^{-21} \text{ cm}^2$ (Chang et al. 2015), meaning that the Raman scattering optical depth through the ionization front is only of order 0.001. A vastly larger column density of neutral hydrogen ($\approx 10^{21} \text{ cm}^{-2}$) is available in the photodissociation region (PDR) outside the ionization front, so it is more likely that Raman scattering will occur there instead, so long as there is sufficient far ultraviolet radiative flux.

This paper is organized as follows. § 2 presents archival VLT-MUSE integral field spectroscopy of the Orion Nebula, which allows the broad H α wings to be spatially mapped in unprecedented detail and compared with other tracers of ionized and neutral zones

* w.henney@irya.unam.mx

in the nebula. Two components of the O I UV resonance multiplet $2p^4 \ ^3P \rightarrow 3d \ ^3D^0$ are detected as absorption features at 6633 and 6664 Å against the H α Raman wings. § 3 presents archival Keck-HIRES slit spectroscopy, which shows the profile of the 6664 Å absorption line with an effective velocity resolution of 1 km s^{-1} . § 4 discusses the implications of these results for the structure and dynamics of the PDRs in Orion, together with the prospects for using Raman spectral mapping as a diagnostic tool in the study of other high-mass star formation regions. An appendix recapitulates the basic theory of Raman scattering, concentrating on the wavelength transformation from the FUV domain around Ly β to optical domain around H α . In addition, polynomial fits are provided to the wavelength dependence of the total (Rayleigh plus Raman) scattering cross section and the Raman H α branching ratio.

2 SPECTRAL MAPPING OF RAMAN WINGS

The principal observational dataset used in this paper is the imaging spectroscopy mosaic of the inner Orion Nebula (Weilbacher et al. 2015; Mc Leod et al. 2016) obtained with the MUSE spectrograph (Bacon et al. 2010, 2014) on the VLT. The entire datacube covers the wavelength range 4595 to 9366 Å but we concentrate mainly on the range 6300 to 6800 Å, where the spectral resolving power is $R \approx 2500$, corresponding to an instrumental linewidth (FWHM) of $\delta\lambda \approx 2.4 \text{ Å}$, which is sampled at 1.25 Å pix^{-1} and then resampled to 0.85 Å pix^{-1} for the final calibrated cube (see § 2 of Weilbacher et al. 2015). The observed field is shown by the white rectangle in Figure 2(a) and includes the entire inner Huygens region of the nebula, which accounts for roughly half of the total radio continuum flux from the H II region (Subrahmanyam et al. 2001). The full datacube is a mosaic that combines observations from 30 separate pointings, with a pixel size of $0.2 \times 0.2''$.

2.1 Raman scattered H α wings

Extended wings to the H α line are detected over the entire map, but they are particularly prominent in the six regions marked as white boxes in Figure 2(b). These are all bar-like features (O'Dell & Yusef-Zadeh 2000; García-Díaz & Henney 2007), which correspond to filamentary ionization fronts. Extracted MUSE spectra around the H α line for each of these regions are shown in Figure 3. All regions show broad wings to the H α line extending from 6300 to 6700 Å, which are consistent with the higher spectral resolution ($R = 7000$) results of Dopita et al. (2016) for the region indicated by a dashed box in Figure 2(b). The continuum is interpolated under the wings by fitting a second-order polynomial to clean regions of the spectra in the ranges 6070 Å to 6225 Å and 6760 Å to 6820 Å, as shown by the lower edge of the gray shading for each spectrum. The continuum is a combination of Paschen recombination emission from hydrogen, which increases to the red, and dust-scattered starlight and two-photon hydrogen emission, which both increase to the blue. The combined F_λ is approximately flat for all regions except the Orion Bar, where dust scattering of the nearby star θ^2 Ori A dominates, resulting in a blueward rise. All of these continuum processes are expected to be smooth on a 100 Å scale,¹ but nonetheless

¹ The only exception is the dust-scattered H α line from the stellar photospheres and winds, but this is confined within $\pm 30 \text{ Å}$ of the rest wavelength (see Fig. 2 of Simón-Díaz et al. 2006) and so does not affect the Raman wings, which are broader than that.

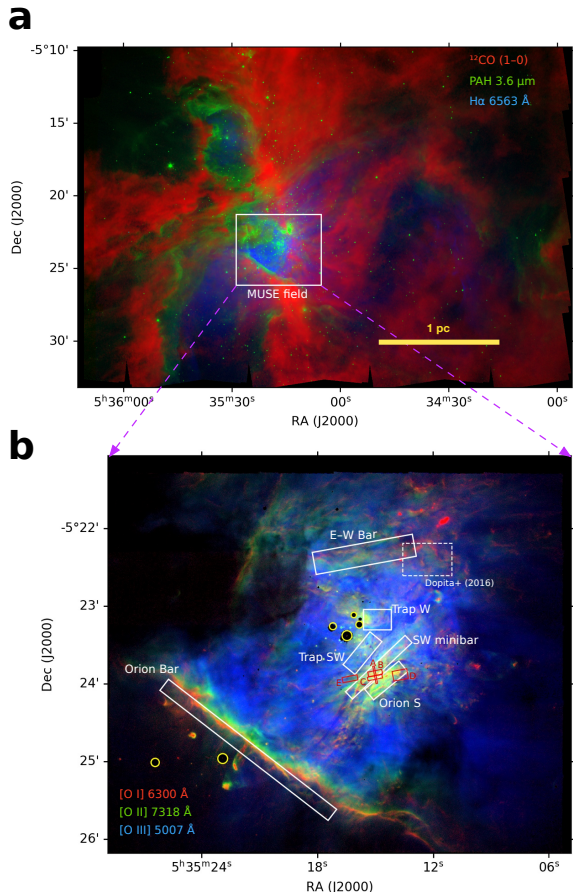


Figure 2. (a) Panoramic view of the Orion Nebula region on parsec scales. Red channel of background image shows ^{18}CO emission from dense molecular gas (Carma-NRO Orion Survey, Kong et al. 2018). Green channel shows near-infrared continuum from PAH grains in neutral gas (Spitzer Orion Survey, Megeath et al. 2012). Blue channel shows optical H α emission from ionized gas (WFI camera on ESO 2.2 m La Silla, Da Rio et al. 2009). The white box shows the field of view observed with MUSE. (b) Locations within the nebula of the extraction regions for the MUSE spectra shown in Figure 3 (white boxes) and the Keck HIRES spectra shown in Figure 10 (red boxes). The region of the spectrum obtained in Dopita et al. (2016) is shown by the dashed box. Background image shows oxygen emission lines extracted from the MUSE data cube: [O I] $\lambda 6300$ (red channel), which traces ionization fronts and shocks in neutral gas; [O II] $\lambda 7318$ (green channel), which traces the outer layers of the photoionized nebula; and [O III] $\lambda 5007$ (blue channel), which traces the highly ionized interior of the nebula.

the systematic uncertainties in the continuum interpolation is an important factor that limits the precision of the Raman wing measurements.

2.2 Raman scattered FUV absorption lines

A prominent feature of all the spectra in Figure 3 is a pair of absorption notches in the red wing at 6633 Å and 6664 Å, which closely correspond to the wavelengths expected for the Raman-scattered transformation of the O I resonance lines at 1027 Å and 1028 Å listed in Table A1. After correcting for instrumental broadening, the FWHM of the 6633 Å feature is $\approx 2.5 \text{ Å}$, which would correspond to a velocity width of 115 km s^{-1} if it were an optical absorption line. However, taking into account the wavelength transformation during

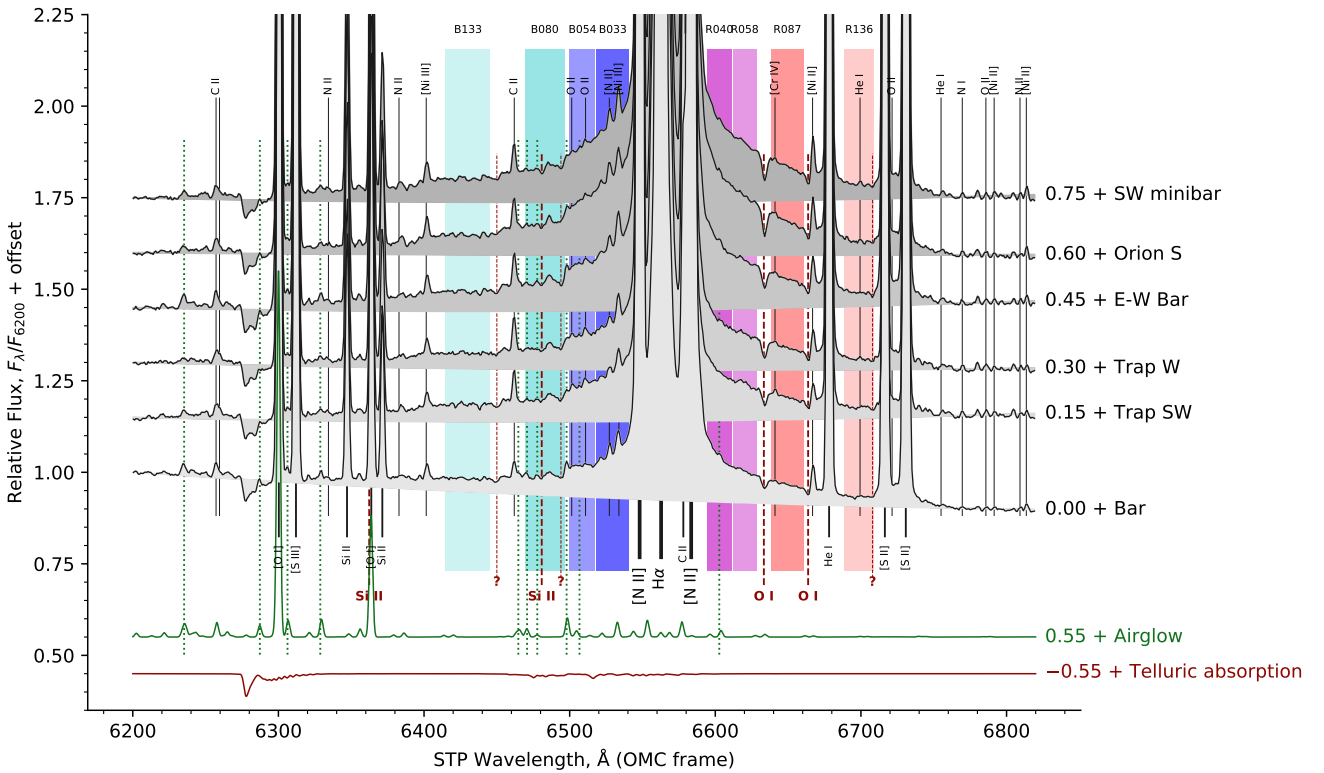


Figure 3. MUSE spectra of the Orion Nebula centered on the $\text{H}\alpha$ line, showing the broad Raman-scattered wings. Spectra are shown for the regions outlined by white boxes in Figure 2 and were extracted from the datacubes of Weilbacher et al. (2015). All spectra are normalized to the continuum at 6200 \AA and are offset vertically as labelled at right. Emission line identifications are shown by solid vertical lines, labelled above for weak lines and below for stronger lines. Wavelengths of Raman-scattered O I and Si II absorption lines from Table A1 are shown by red dashed vertical lines, labelled in bold font below, together with unidentified candidate absorption features marked with “?”. Dotted lines show night sky lines identified in the Dark Bay region of the nebula. At the bottom of the figure are shown the theoretical upper-atmosphere airglow spectrum (green line) and telluric molecular absorption spectrum (red line), as calculated from the Cerro Paranal Advanced Sky Model (Noll et al. 2012; Moehler et al. 2014).

Raman scattering (eq. [A2]), the true velocity width of the FUV line is 18 km s^{-1} . The absorption depth of the features is roughly 50% with respect to the Raman-scattered wing at adjacent wavelengths, but is much less than this with respect to the total continuum emission. The same spectral features are also visible in the Dopita et al. (2016) spectra but are not commented on by those authors. The 6664 \AA feature is partially blended with the $[\text{Ni II}] 6666.8 \text{ \AA}$ nebular emission line in the MUSE spectra, but these are better resolved in the higher resolution Dopita et al. spectra. Archival Keck HIRES observations of this feature at an even higher spectral resolution are presented below in § 3. The identification of these two FUV absorption lines in the optical spectrum is incontestable proof of a Raman scattering origin for the broad $\text{H}\alpha$ wings.

There is also evidence for a weak absorption feature in the blue wing at 6481 \AA , corresponding to the Si II absorption line at 1024 \AA . However, the blue wing is much less clean than the red wing, partly due to telluric absorption and airglow emission (see below), which makes the identification uncertain. The Raman wings show some other weak features that remain unidentified, the strongest of which is an apparent broad ($\approx 5 \text{ \AA}$) absorption feature at 6494 \AA , while additional narrower features are seen at 6450 \AA and 6708 \AA (all marked with “?” in Figure 3). It is not clear if these are truly absorption features or whether they are simply gaps between very weak blended emission lines.

2.3 Definition of observational Raman bands in the red and blue wings

In order to study the spatial distribution of the Raman-scattered wings, it is convenient to define a series of broad bands on the blue and red sides, which are listed in Table 1 and shown as blue and red shaded vertical stripes in Figure 3. Four bands are defined in each wing, spanning a range in $|\Delta\lambda_2|$ from about 30 \AA to 150 \AA . The lower limit of this range is determined by overlap with the strong nebular $[\text{N II}]$ emission lines, while the upper limit is due to the $[\text{S II}]$ lines on the red side, combined with the Raman wings becoming too weak to measure. The mean H^0 $\text{Ly}\beta$ cross section corresponding to each band (eq. [A5]) is also given in the table, varying between 10^{-22} cm^2 and $2 \times 10^{-21} \text{ cm}^2$.

The bands are chosen so as to avoid the strongest contaminating lines wherever possible, but some small contamination is unavoidable, as listed in the rightmost column of the table. The contamination comes from two sources: weak nebular emission lines (indicated by solid vertical lines in Figure 3) and additionally from the line absorption and emission of the Earth’s atmosphere. Two complementary methods were used to investigate this latter effect. First, the datacube was inspected to identify lines with roughly uniform brightness across the entire map. In particular, any line that is as strong in the Dark Bay region as it is in Orion S is unlikely to come from the nebula itself. Such lines are indicated by vertical

Table 1. Wavelength bands used for Raman wing extraction

	Band (1)	$\langle \Delta\lambda_2 \rangle$, Å (2)	λ_{\min} , Å (3)	λ_{\max} , Å (4)	$f_{H\alpha}$ (5)	$\langle \sigma_\lambda \rangle, 10^{-21} \text{ cm}^2$ (6)	Contamination (7)
Blue wing	B133	-132.8	6414.85	6445.45	0.180	0.144	
	B080	-79.5	6469.25	6496.45	0.196	0.378	Sky 6471, 6478, H ₂ O
	B054	-53.6	6499.85	6517.70	0.205	0.802	O II? 6502, 6510, Sky 6507, H ₂ O
	B033	-32.8	6518.55	6540.65	0.212	2.069	[N II] 6527.24, [Ni III] 6533.76, H ₂ O
Red wing	R040	40.3	6594.20	6611.20	0.238	1.451	Sky 6603
	R058	57.7	6612.05	6628.20	0.244	0.695	
	R087	87.1	6638.40	6660.50	0.255	0.299	[Cr IV]? 6641
	R136	135.7	6688.55	6708.95	0.274	0.119	He I 6699

COLUMNS: (1) Name of band. (2) Mean wavelength displacement from H α rest wavelength. (3, 4) Upper and lower wavelength limits for the band. (5) Mean value of the H α branching ratio from virtual 3p levels (see equation [A6]). (6) Mean value of Ly β wing cross-section that can feed this band via Raman scattering (see equation [A5]). (7) Nebular and telluric lines that may contaminate the band (see text for details).

dotted lines in Figure 3 and some are listed in Table 1. Second, ESO’s SkyCalc tool² was used to predict theoretical emission and absorption spectra for the atmosphere above the VLT at the time and airmass of the observations, convolved with the MUSE instrumental profile. The emission spectrum is dominated by upper-atmosphere airglow lines of OH (Osterbrock et al. 1996; Noll et al. 2012, 2014), shown in green in the figure, many of which can be seen to coincide with the empirically determined sky lines. The absorption spectrum is dominated by telluric lines of O₂ and H₂O (Moehler et al. 2014; Smette et al. 2015). The strongest predicted absorption near H α is the O₂ γ band at 6280 Å, which is clearly seen in all the spectra, with an absorption depth of order 0.1, but lies well away from the Raman wings. The blue Raman wing is affected by weaker H₂O bands at 6460 Å to 6600 Å with absorption depth < 0.01, as compared to the relative brightness of the Raman wings at those wavelengths, which is 0.05 to 0.1.

In summary, the nebular and telluric contamination introduces uncertainties of order 10% in the fluxes of the B033, B054, and B080 bands, with other bands being affected to a much lesser degree.

2.4 Spatial distribution of Raman band emission

Figure 4 shows maps of the six innermost Raman bands as two RGB images: the blue wing in panel a and the red wing in panel b. In each case, the channel sequence R, G, B is an inward progression towards line center, from the farther wings to the nearer wings. The maps are adaptively smoothed following the binary grid algorithm outlined in García-Díaz et al. (2018), which reduces the noise in the fainter regions at the cost of a reduced spatial resolution. The two maps are strikingly similar, indicating that the contamination of the blue wing (see previous section) is indeed a minor effect when integrated over an entire band.

To aid in the interpretation of the Raman wing maps, Figure 4c shows a combined view of mid-to-low-ionization oxygen emission lines, derived from the MUSE data cube. In blue is shown the [O II] 7318.39, 7319.99 Å doublet, which traces the outer 10% of the fully ionized emission. In green is shown the [O I] 6300.30 Å line, which principally traces partially ionized gas at the ionization front, but also shocks in neutral gas. In red is shown the fluorescent O I 8446.36 Å line, which traces fully neutral gas that is very close behind the ionization front. This image clearly illustrates that the

neutral/molecular gas is organized in filaments, with bright ionization fronts on the side facing the high-mass Trapezium stars. This is most clearly seen in the Orion Bar, the linear emission feature to the south-east of the map, but analogous filaments are seen in all directions from the Trapezium (see also Figure 2b). A particularly complex region, with several partially overlapping filaments, lies between the Trapezium and the Orion S star formation region. This region shows the brightest Raman wing emission, suggesting that it contains the neutral gas with the highest incident FUV flux, presumably because it lies physically closest to the illuminating high-mass stars.

The spatial relation of the Raman-scattered wings to other emission lines is illustrated in Figure 4d, which shows the summed wing intensity over all 8 bands as a false color scale. This is compared with contours that show the ionization front, as traced by the collisionally excited [O I] line, and molecular gas, as traced by the optically thick ¹²CO (1–0) line (Kong et al. 2018). In the Bar region, the Raman emission is clearly seen to be sandwiched between the ionization front and the molecular gas, conclusive evidence that it arises in the neutral zone of the PDR. In the Orion S region and around the Trapezium, there is not such a clear stratification between ionized, neutral, and molecular emission. This is due to two factors: first, the densities are higher, which shortens all length scales, and second, the geometry is not so edge-on, leading to a greater degree of superposition along the line of sight, as witnessed by the overlap of the [O I] and ¹²CO contours. Nonetheless, even here there is evidence that the Raman emission tends to lie farther from θ¹ Ori C than the ionization front, particularly in the “SW minibar” region.

2.5 Emission profiles across the Orion Bar

Figure 5 shows spatial profiles across the Orion Bar of the Raman-scattered bands (panel a), together with other emission lines and bands (panels b and c). In keeping with the dominant tradition in the literature (e.g., Fig. 9 of van der Werf et al. 1996, Fig. 2 of Goicoechea et al. 2017), the molecular regions are shown on the left and the ionized regions on the right. The profiles are the median values across a slit of width 75'', as illustrated in Figure 5d. Table 2 shows the positions, widths, and intensities of the peaks in each tracer, as determined by fitting a single Gaussian plus a linear background.

² <http://www.eso.org/sci/software/pipelines/skytools/skycalc>



Figure 4. Spatial distribution of Raman-scattered wings of H α . (a) Three-color RGB image of bands in the blue wing: B080 (red channel), B054 (green), B033 (blue). All bands are continuum-subtracted and are multibinned at constant signal-to-noise (see text). Maximum brightness in the (red, green, blue) channels is $(2.27, 3.89, 7.78) \times 10^{-9} \text{ erg s}^{-1} \text{ cm}^{-2} \text{ sr}^{-1} \text{ Å}^{-1}$. The brightest stars are masked out and marked with yellow circles. Lower-mass stars are not masked and most appear as yellow/red dots. (b) Same as (a) but for bands in the red wing: R087 (red), R057 (green), R040 (blue). (c) Three-color RGB image of collisional and fluorescent oxygen emission lines that bracket the ionization front: O I $\lambda 8446 \text{ Å}$ (red), [O I] $\lambda 6300 \text{ Å}$ (green), [O II] $\lambda 7318 \text{ Å}$ (blue). Various features of the nebula are marked, including Herbig-Haro objects driven by jets from young stars. (d) Comparison of the total Raman wing intensity (blue-to-yellow false color image) with the [O I] emission that traces the ionization front (orange contours) and ^{12}CO emission that traces molecular gas (red, purple, and blue contours for different LSR velocities as marked).

2.5.1 Lines from ionized gas and the ionization front at the Bar

The ionization stratification at the edge of the H II region is clearly seen in the distribution of the [O III], [O II], [O I], and O I lines (Fig. 5c). The peak in [O I] emissivity (excited by collisions between electrons and neutral oxygen atoms) is expected to occur at a hydrogen ionization fraction of 50% (Henney et al. 2005), which is displaced by $x_0 \approx -1.7 \text{ mpc}$ from the peak of the O I fluorescent line. This latter should correspond to an absorption optical depth of approximately unity in the FUV pumping lines, such as those listed in Table A1 (see § 5 of Walmsley et al. 2000), corresponding to a neutral hydrogen column density of $N(\text{H}^0) \approx 10^{19} \text{ cm}^{-2}$ and therefore an average volume density of $n(\text{H}^0) = N(\text{H}^0)/|x_0| \approx 2000 \text{ cm}^{-3}$. This value is similar to the peak electron density on the fully ion-

ized side of the ionization front: $n_e \approx 3000 \text{ cm}^{-3}$, measured from the [S II] 6717/6731 ratio (e.g. O'Dell et al. 2017), which occurs at $x \approx -7 \text{ mpc}$, close to the peak in the [O II] emission. Therefore, the total hydrogen density is roughly constant over the transition between a predominantly ionized state and predominantly neutral state. Note that the apparent width of this transition (for instance, the FWHM of the [O I] peak $\approx 9 \text{ mpc}$) is much larger than predicted by atomic physics, which is probably due to spatial irregularities in the ionization front, which can be seen in the inset Figure 5d and is discussed in more detail in § 4.5 below.



Figure 5. (a) Spatial cut of continuum-subtracted H α wing intensity across the Orion Bar. Matched band pairs from the red and blue wings are shown with the same color scheme as in Fig. 3. (b) Comparison with far-infrared observations of line and continuum (purple shading) emission from Herschel PACS (Bernard-Salas et al. 2012). The width (FWHM) of the Herschel PSF is shown by horizontal bars for two representative wavelengths. (c) Comparison with a variety of other tracers of molecular, neutral, and ionized material. Optical lines are from VLT MUSE (Weilbacher et al. 2015), infrared continuum bands (green shading) are from Spitzer IRAC (Megeath et al. 2012), CO lines are from CARMA-NRO (Kong et al. 2018) and Herschel PACS (Parikka et al. 2018), H $_2$ near-infrared line is from VLT HAWK-I (Kissler-Patig et al. 2008). (d) Image of the bar in O 1 , rotated so the x axis is along the direction of the spatial cuts (area indicated by dashed rectangle). Contours of molecular CO emission (red) and ionized [O III] emission (blue) are also shown. In all four panels, ultraviolet photons are incident from the right hand side and the vertical dotted line indicates the ionization front, defined as the peak of the fluorescent O 1 emission. The profiles are the median values over a slit width of $75''$, centered on the ICRS equatorial coordinates $\alpha = 83.8419^\circ$, $\delta = -5.4113^\circ$ and oriented at a position angle of 141.5° . Distances from the ionization front are given in mpc where $1'' \approx 1.9 \text{ mpc}$ for an assumed distance of $(388 \pm 5) \text{ pc}$ (Kounkel et al. 2017).

Table 2. Peaks in emission profiles across the Orion Bar

Emission type and units (1)	Line or Band (2)	x_0 , mpc (3)	δx , mpc (4)	$I(\text{Peak})$ (5)	$I(\text{BG})$ (6)	Ref. (7)
H II region emission lines	[O III] $\lambda 5007$	-32.1 ± 2.6	45	13.059	11.642 ± 5.605	1
	[O II] $\lambda 7318$	-9.4 ± 3.6	25	0.882	0.232 ± 0.026	1
Peak and BG: $\int I_\lambda d\lambda, 10^{-6} \text{ erg s}^{-1} \text{ cm}^{-2} \text{ sr}^{-1}$	[O I] $\lambda 6300$	-1.7 ± 0.1	9	0.152	0.045 ± 0.001	1
	O I $\lambda 8446$	0.0 ± 0.8	8	0.226	0.071 ± 0.000	2
H α Raman bands	B033	0.8 ± 1.5	20	0.455	0.858 ± 0.007	2
	R040	1.8 ± 0.1	18	0.480	0.815 ± 0.023	
Peak and BG: $I_\lambda, 10^{-9} \text{ erg s}^{-1} \text{ cm}^{-2} \text{ sr}^{-1} \text{ Å}^{-1}$	B054	5.0 ± 2.7	9	0.233	0.641 ± 0.009	
	R058	5.5 ± 2.8	11	0.285	0.591 ± 0.017	
	B080	7.1 ± 1.3	11	0.136	0.437 ± 0.013	
	R087	7.1 ± 0.7	15	0.178	0.393 ± 0.017	
	B133	6.7 ± 1.1	10	0.128	0.302 ± 0.004	
	R136	3.1 ± 2.7	27	0.072	0.198 ± 0.007	
Spitzer IRAC bands	$3.6 \mu\text{m}$	11.6 ± 1.1	21	0.200	0.182 ± 0.018	3
Peak and BG: $I_\nu, \text{GJy sr}^{-1}$	$5.8 \mu\text{m}$	12.8 ± 2.4	23	1.702	0.966 ± 0.073	
	$8.0 \mu\text{m}$	13.9 ± 3.4	24	4.866	2.622 ± 0.119	
Herschel PACS continuum	$60 \mu\text{m}$	23.9 ± 7.0	52	66.361	25.175 ± 0.261	4
Peak and BG: $I_\nu, \text{Jy pix}^{-1}$	$150 \mu\text{m}$	39.2 ± 4.2	63	7.263	2.592 ± 0.065	
PDR emission lines	[N II] $122 \mu\text{m}$	-4.0 ± 1.7	55	1.907	0.581 ± 0.181	4
	[O I] $63 \mu\text{m}$	21.6 ± 1.2	55	1.303	0.823 ± 0.242	4
Peak and BG: $\int I_\lambda d\lambda$, median normalized	$\text{H}_2 2.12 \mu\text{m}$	23.6 ± 0.1	19	0.169	0.997 ± 0.002	5
	[C II] $158 \mu\text{m}$	24.3 ± 1.9	47	0.975	0.920 ± 0.145	4
	[O I] $146 \mu\text{m}$	26.0 ± 2.8	46	2.299	0.945 ± 0.210	4
	$^{12}\text{CO} (19-18)$	33.8 ± 0.1	32	3.930	0.399 ± 0.001	6
	[C I] $\lambda 8727$	37.7 ± 5.9	30	0.495	0.854 ± 0.122	2
	$^{12}\text{CO} (18-17) 145 \mu\text{m}$	38.9 ± 0.5	34	8.193	0.989 ± 0.154	4
	$^{12}\text{CO} (1-0)$	41.1 ± 1.2	44	0.472	0.746 ± 0.173	7
	$^{13}\text{CO} (1-0)$	49.8 ± 2.1	33	0.891	0.823 ± 0.112	7

NOTE—Results of fitting a single Gaussian plus linear background to the brightness profiles shown in Figure 5. COLUMNS: (1) Type of tracer and surface brightness units for the values given in columns 5 and 6. (2) Specific emission line or continuum band. (3) Peak position of fitted Gaussian relative to ionization front. Negative values are on the ionized side of the front, positive values on the neutral/molecular side. The uncertainty is determined as the difference between the fitted Gaussian peak and the actual data peak. (4) FWHM of fitted Gaussian. Note that this is not corrected for the instrumental PSF, which contributes at the 10–20% level in the case of the Herschel and CARMA data (references 4 and 7) but is negligible in other cases. (5) Peak intensity of fitted Gaussian, with brightness units given in column 1. (6) Intensity of fitted background at position $x_0 \pm \delta x$. (7) Data provenance references: 1. VLT–MUSE (Weilbacher et al. 2015); 2. VLT–MUSE (this paper); 3. Spitzer–IRAC (Megeath et al. 2012); 4. Herschel–PACS (Bernard-Salas et al. 2012); 5. VLT–HAWK-I (Kissler-Patig et al. 2008); 6. Herschel–PACS (Parikka et al. 2018); 7. Carma–NRO (Kong et al. 2018).

2.5.2 Spatial profiles of the Raman bands in the neutral Bar

Unlike the optical emission lines, the Raman wing bands (upper panel of Fig. 5) all show peaks at positive values of x , corresponding to fully neutral gas in the PDR. There is a very close agreement between corresponding pairs of blue and red bands: B033 with R040, B054 with R058, and B080 with R087. However, there is a systematic tendency for the blue band intensity to be slightly higher than its red counterpart on the ionized side (negative values of x), which is probably due to contamination by nebular emission lines, as listed in column 7 of Table 1. There is a clear tendency for the peak in the brightness profile to progress towards greater depths into the neutral gas as one moves to wavelengths farther from the H α line center, which is quantitatively confirmed by the Gaussian fits in Table 2. This result is used as a diagnostic of the PDR density in § 4.2.3 below.

2.5.3 Other PDR tracers of the neutral and molecular Bar

The left hand side of panels b and c of Figure 5 show a variety of other emission lines and continuum bands, which trace different

layers in the PDR. The near-infrared H $_2 v = 1 \rightarrow 0$ S(1) line marks the hydrogen dissociation front at $x_0 \approx 24$ mpc (van der Werf et al. 1996; Luhman et al. 1998; Marconi et al. 1998), which provides the outer boundary of the neutral hydrogen layer. Beyond this are found the high- J CO lines, which trace the CO dissociation front at $x_0 \approx 36$ mpc. These coincide with near-infrared [C I] emission, which mainly traces the recombination of C $^+$ ions in cool gas near the dissociation front (Escalante et al. 1991). The mm-band CO lines trace the deeper, fully molecular regions, with the optically thick $^{12}\text{CO} (1-0)$ line at $x_0 \approx 41$ mpc arising outside of the optically thin $^{13}\text{CO} (1-0)$ line at $x_0 \approx 50$ mpc (Kong et al. 2018).

The broad infrared bands are dominated by dust emission. For the case of the 3.6 to $8.0 \mu\text{m}$ *Spitzer* bands (Megeath et al. 2012), mid-infrared spectroscopy (Bregman et al. 1989; Cesarsky et al. 2000; Kassis et al. 2006) shows that they are mainly due to discrete polycyclic aromatic hydrocarbon (PAH) features at 3.3, 6.2, 7.7, and $8.6 \mu\text{m}$, plus a continuum contribution from very small grains (VSGs, with size $a \sim 0.007 \mu\text{m}$, Desert et al. 1990) and minor contributions from ionized gas lines such as [Ar II] and [Ar III]. The longer wavelength 60 and $150 \mu\text{m}$ *Herschel* bands (Bernard-Salas et al. 2012) show continuum emission from larger grains

($a \sim 0.1 \mu\text{m}$). The peak of the dust emission moves deeper into the PDR with increasing wavelength, reflecting the decreasing dust temperature as the stellar radiation field is attenuated (Arab et al. 2012).

A complementary view of the Bar is provided by far-infrared emission lines of neutral and ionized metals observed by *Herschel* (Bernard-Salas et al. 2012). The [N II] 122 μm line comes from the H⁺ region and shows a similar distribution to the optical [O II] line. The [C II] 158 μm and [O I] 63 and 146 μm lines, on the other hand, come from the H⁰ region of the PDR.

2.6 Equivalent widths of absorption features

Figure 6 shows grayscale maps of the observed equivalent widths, W_λ^{obs} , of various absorption features that are found superimposed on the continuous spectrum of the Orion Nebula. These are extracted from the MUSE datacubes by integrating over a short wavelength interval, $\Delta\lambda = \pm 8 \text{ \AA}$, around the central wavelength of the absorption feature:

$$W_\lambda^{\text{obs}} = \int_{\Delta\lambda} \frac{I_{\lambda,\text{cont}} - I_\lambda}{I_{\lambda,\text{cont}}} d\lambda \text{ \AA}, \quad (1)$$

where $I_{\lambda,\text{cont}}$ is the continuum intensity, which is interpolated from the absorption-free portions of the $\Delta\lambda$ interval.

2.6.1 Raman-scattered O I 1027 \AA

Figure 6a shows W_λ^{obs} for the 6633 \AA absorption feature, which is a candidate for being a Raman-scattered FUV absorption line. Note that in this case, the ‘‘continuum’’ intensity $I_{\lambda,\text{cont}}$ includes a contribution from the broad Raman wing, as well as the ‘‘true’’ nebular continuum and dust-scattered starlight. Due to the weakness of both the continuum and the absorption line, it was necessary to aggressively bin the data in order to produce an acceptable map. The results in Figure 6d are for a minimum S/N of 7 in W_λ^{obs} , which gives the optimum balance between noise and spatial resolution.

The 6633 equivalent width is non-zero across the entire map, with a median value of $W_\lambda^{\text{obs}}(6633) \approx 0.1 \text{ \AA}$. It shows peaks of $W_\lambda^{\text{obs}}(6633) = (0.3 \pm 0.1) \text{ \AA}$ in exactly the same areas as the peaks in the Raman band emission (see § 2.4). For ease of comparison, Figure 6d shows a map of the wing-to-continuum ratio, R_{wing} , for the R087 red Raman wing band, which is found by dividing the continuum-subtracted intensity in the MUSE data cube by the intensity of the interpolated continuum:

$$R_{\text{wing}} = \frac{\int_{\lambda_{\min}}^{\lambda_{\max}} (I_\lambda - I'_{\lambda,\text{cont}}) d\lambda}{\int_{\lambda_{\min}}^{\lambda_{\max}} I'_{\lambda,\text{cont}} d\lambda}, \quad (2)$$

where the band limits λ_{\min} , λ_{\max} are given in Table 1. In this case, the continuum intensity $I'_{\lambda,\text{cont}}$ does *not* include the Raman wing emission since it is interpolated across a much wider range than in equation (1) by fitting a quadratic function to clean sections of continuum around $(6150 \pm 80) \text{ \AA}$ and $(6790 \pm 30) \text{ \AA}$ (see § 2.1). Note also that R_{wing} is a dimensionless ratio, whereas W_λ^{obs} has dimensions of wavelength. The reason for choosing the R087 band for this figure is that it is the band that is closest in wavelength to the 6633 \AA absorption feature. It is clear from comparing Figure 3 panels a and d that $W_\lambda^{\text{obs}}(6633)$ and R_{wing} closely track one another, as would be expected if the absorption feature is the Raman-scattered O I 1027 \AA line.

The relationship is examined more quantitatively in Figure 7, which shows that $W_\lambda^{\text{obs}}(6633)$ and R_{wing} are well-correlated, with a

mean slope of $W_\lambda = 2.27 R_{\text{wing}}$. Of the six extraction regions used in Figure 3, only the Orion Bar lies on this mean relation. The other regions, which are closer to the Trapezium (see Figure 2b) follow a slope that is roughly 50% steeper. Although this might represent a real physical difference, it is also true that the lower-left area of the graph in Figure 7 is more susceptible to systematic errors. For instance, in the Orion Bar region much of the continuum comes from the blue reflection nebula around θ^2 Ori A, which causes increased spectral curvature (see Figure 3), potentially leading to reduced accuracy in the continuum interpolation, which might result in an overestimation of R_{wing} . Higher values of R_{wing} and W_λ , such as those seen in Orion S, are much less affected by such uncertainties.

2.6.2 Stellar absorption lines

Figure 6b and e show W_λ^{obs} for the He II 4685.68 \AA absorption line and the C IV 5801.35, 5811.97 \AA doublet, respectively. Neither of these lines are expected to be seen in emission from the photoionized gas in the nebula due to the high ionization potentials required. They are therefore well-suited for tracing the diffuse dust-scattered starlight in the nebula. It can be seen that the distribution of the two lines is very different. For the He II line, one finds $W_\lambda^{\text{obs}}(4686) \approx 0.2 \text{ \AA}$ across most of the nebula, but with consistently larger values to the SE, with a pronounced peak of $W_\lambda^{\text{obs}}(4686) = (0.4 \pm 0.1) \text{ \AA}$ around the star θ^2 Ori A. In addition, there is a secondary peak of $W_\lambda^{\text{obs}}(4686) = (0.30 \pm 0.05) \text{ \AA}$, located close to θ^1 Ori D, the easternmost of the four Trapezium stars. In contrast, the C IV lines show a broad maximum of $W_\lambda^{\text{obs}}(5801 + 5812) = (0.16 \pm 0.04) \text{ \AA}$, centered to the SW of the Trapezium.

The most straightforward of these to interpret is C IV, since the 5801,5812 doublet is present in the spectrum of θ^1 Ori C, with a summed equivalent width $W_\lambda^\star = (0.44 \pm 0.04) \text{ \AA}$ (Stahl et al. 1996)³, but is absent in all the other OB stars in the nebula (as measured from the MUSE datacube). The equivalent width observed in the nebula is smaller than this, because of dilution by the nebular continuum (recombination plus 2-photon) and the starlight from the lower mass members of the Trapezium cluster. The fraction of the total observed continuum intensity that is due to dust-scattering of θ^1 Ori C can be estimated as $f_{\text{scat}} = W_\lambda^{\text{obs}} / W_\lambda^\star$, for which we find a maximum value of $f_{\text{scat}}(\theta^1 \text{ Ori C; C IV}) = 0.4 \pm 0.1$ in the region between the Trapezium and Orion S.

Although θ^1 Ori C (spectral type O7V f?p var; Simón-Díaz et al. 2006; Maíz Apellániz et al. 2019) is the hottest and most luminous star in the nebula, its He II 4686 absorption line is anomalously weak and varies markedly on a rotational timescale of 15.4 days (Conti 1972; Stahl et al. 1993) because it is partially filled in by emission from the magnetosphere and complex magnetically-channelled stellar wind (Donati et al. 2002). From Fig. 5 of Stahl et al. (1996), it can be seen that $W_\lambda^\star(\theta^1 \text{ Ori C; 4686})$ varies systematically from -0.1 \AA to 0.4 \AA as a function of rotational phase.⁴ Three-dimensional simulations (ud-Doula et al. 2013) show that the line profile is dominated by emission ($W_\lambda^\star < 0$) for viewing directions along the magnetic pole, but by photospheric absorption ($W_\lambda^\star > 0$) for viewing directions in the magnetic equator. Comparison with observed phase-dependent line profiles suggests

³ The 10% uncertainty is due to variation with rotational phase, see next paragraph.

⁴ Negative equivalent widths correspond to net emission, rather than absorption.

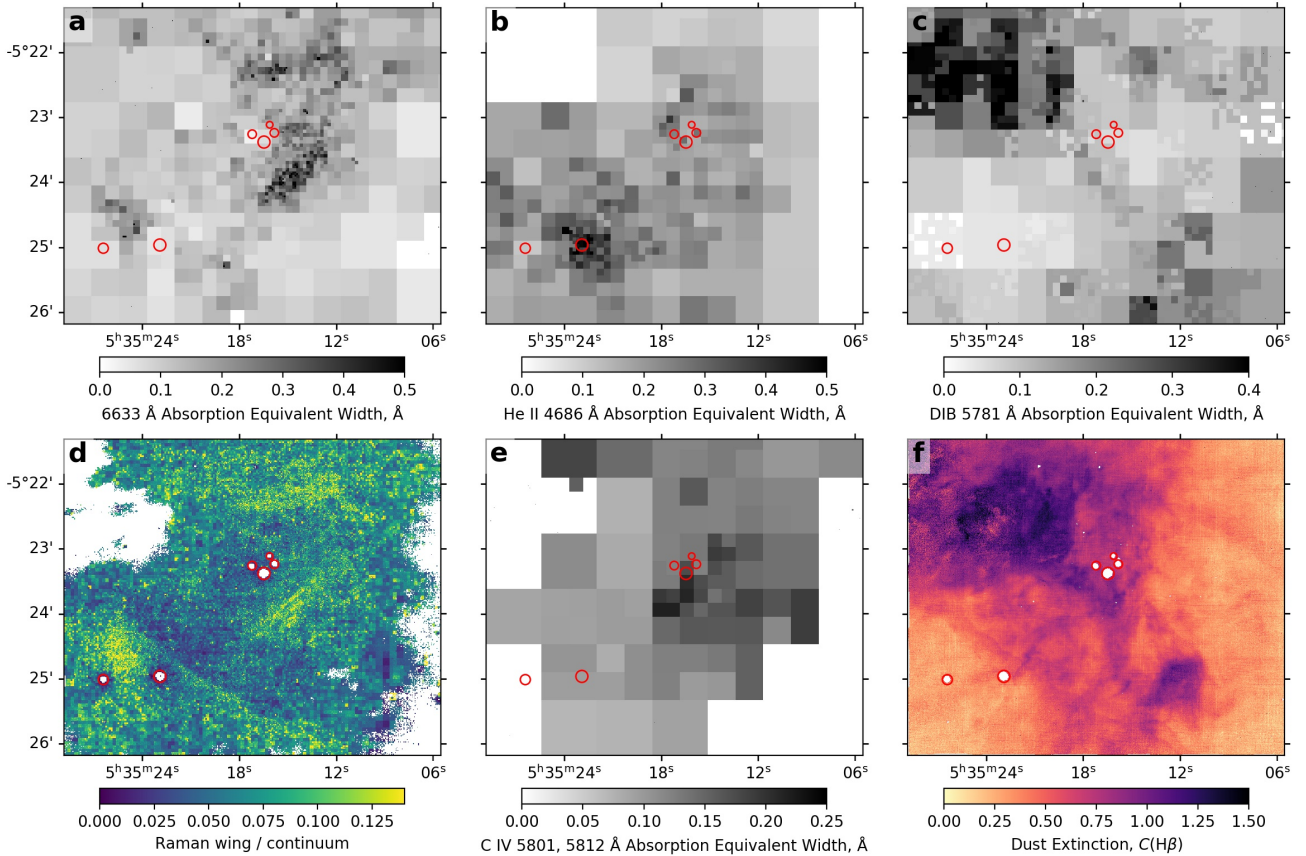


Figure 6. Maps of equivalent widths W_λ^{obs} of different absorption features (grayscale images), compared with maps of other quantities (false color images). Red circles show positions of bright stars, from West to East: θ^1 Ori A, B, C, D, and θ^2 Ori A, B. (a) Equivalent width of 6633 Å absorption feature. (b) Equivalent width of He II 4685.68 Å absorption line. (c) Equivalent width of a solid-state Diffuse Interstellar Band absorption feature at 5781 Å. (d) Ratio R_{wing} of Raman wing intensity (R058 band) to the intensity of the underlying continuum at the same wavelength. (e) Equivalent width of C IV 5801.35, 5811.97 Å absorption line doublet (sum of the two lines). (f) Foreground dust extinction to the ionized gas, $C(H\beta)$ (base-10 logarithmic extinction at 4861 Å), calculated from the Balmer decrement $H\alpha/H\beta$, assuming the reddening curve of Blagrave et al. (2007).

that both the line-of-sight from Earth and the magnetic dipole axis are inclined at $\approx 45^\circ$ from the rotation axis. This implies that the spectrum seen from Earth, integrated over the rotational period, is broadly representative of the average stellar spectrum seen by the surrounding nebula, so that a value of $W_\lambda^*(\theta^1 \text{ Ori C}; 4686) \approx 0.15 \text{ \AA}$ is appropriate, albeit with a large uncertainty.

The second most luminous star in the nebula is the spectroscopic binary θ^2 Ori A (spectral type O9.2V + B0.5:V(n); Maíz Apellániz et al. 2019), located to the SE of the nebula, beyond the Bright Bar. This shows a much simpler He II line profile with $W_\lambda^*(\theta^2 \text{ Ori A}; 4686) = 0.53 \text{ \AA}$ (Simón-Díaz et al. 2006), which explains why $W_\lambda^{\text{obs}}(4686)$ is higher around θ^2 Ori A, than around the Trapezium. Applying the same argument as above yields a maximum value of $f_{\text{scat}}(\theta^2 \text{ Ori A}; \text{He II}) = 0.75 \pm 0.2$, implying that the blue continuum in this area of the nebula is totally dominated by scattered light from θ^2 Ori A, which forms a roughly circular reflection nebula.

The same absorption line is present in the spectra of other Trapezium stars, being strongest in the B0.5V star θ^1 Ori D with $W_\lambda^*(\theta^1 \text{ Ori D}; 4686) \approx 0.25 \text{ \AA}$ (Simón-Díaz et al. 2006). It is therefore interesting and suggestive that the local peak in $W_\lambda^{\text{obs}}(4686)$ is on θ^1 Ori D's side of the Trapezium. This would not be expected if

all the Trapezium stars lay at the same distance from the scattering grains because θ^1 Ori C is 4 times brighter than θ^1 Ori D at visual wavelengths, so the latter star contributes relatively little to the total luminosity of the Trapezium. However, it has been suggested (Smith et al. 2005) that θ^1 Ori D may lie closer to the background molecular gas, roughly 0.1 pc behind θ^1 Ori C. In such a case, it would be possible for θ^1 Ori D to dominate the illumination of a small reflection nebula around itself, and the present results would tend to confirm that.

2.6.3 Solid-state absorption features

A third type of absorption feature found in the nebular spectrum is what is known as Diffuse Interstellar Bands (DIBs; Heger 1922), of which hundreds are now known (Galazutdinov et al. 2000; Hobbs et al. 2008). The majority are believed to be due to large carbon-based molecules associated with atomic gas (Sonnentrucker 2014) but, apart from in a few instances (Cordiner et al. 2019), their exact nature is still uncertain (Tielens 2014; Omont et al. 2019; Lai et al. 2020). The strongest such feature found in the MUSE spectra is the well-known band at 5780 Å, which is shown in Figure 6c. For comparison, the foreground extinction to the nebula is shown in

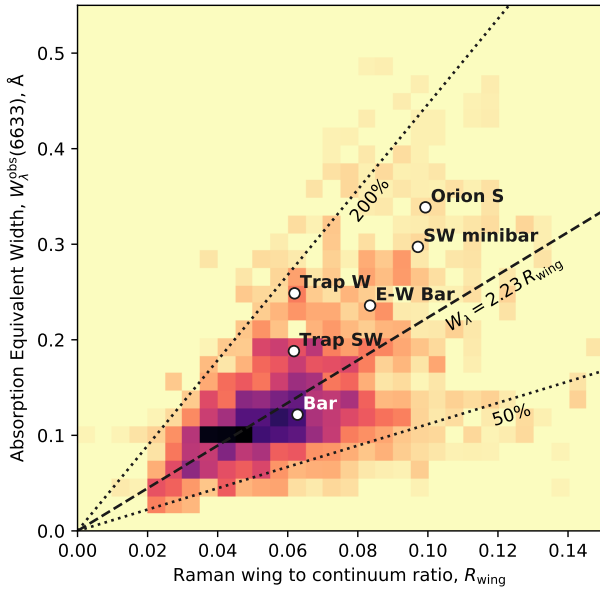


Figure 7. Correlation between 6633 Å equivalent width, $W_\lambda^{\text{obs}}(6633)$, and Raman wing to continuum ratio, R_{wing} . False-color image shows histogram of pixels across the face of the nebula, calculated from the MUSE spectral cube: Fig. 6 panel a (y axis) and panel d (x axis). The histogram is weighted by the 6630 Å continuum intensity. The straight dashed line shows the mean relation, $W_\lambda = 2.27 R_{\text{wing}}$, while dotted lines show a 2× steeper and 2× shallower slope. Symbols show average values for each of the extraction regions shown by white boxes in Figure 2b.

Figure 6f, which is calculated from the H α /H β ratio, assuming the extinction curve of Blagrove et al. (2007).

It is clear at a glance that the spatial distribution of the DIB absorption and the continuum dust absorption are very similar. This is not surprising, since many studies have established a correlation between DIB equivalent widths and interstellar reddening (Friedman et al. 2011; Kos & Zwitter 2013; Baron et al. 2015; Krelowski et al. 2019). This is tested quantitatively in Figure 8, which shows the correlation between $W_\lambda^{\text{obs}}(5780)$ and dust reddening $E(B - V)$. The relative weakness of the 5797 Å DIB feature in all Orion Nebula sight lines is characteristic of σ -type DIBs (after the prototype σ Sco; Krelowski & Westerlund 1988), which tend to be found in atomic diffuse clouds. I therefore compare the results with a fit to 27 σ -type sight lines to OB stars from the survey of Kos & Zwitter (2013) (dotted line in Figure 8), which covers the reddening range $E(B - V) = 0.1$ to 1.2. I also show (dashed line in figure) a fit to over a million stacked external galaxy and quasar sight lines from SDSS (Baron et al. 2015), which cover the reddening range $E(B - V) = 0$ to 0.11. It can be seen that the nebular values follow the general trend of the fits, albeit with considerable dispersion. The tail of high W_λ above the fit lines may be due to the fact that a significant fraction of the continuum is dust-scattered and those photons will have traversed a larger column of dust than is measured by the foreground reddening. In addition, the Balmer decrement will saturate at high column densities if part of the dust is mixed with the emitting gas, resulting in an underestimate of $E(B - V)$.

A further DIB feature is seen in the spectra at 6284 Å. However, it is hard to estimate the equivalent width of this feature since it overlaps with telluric O₂ γ -band absorption (see Figure 3).

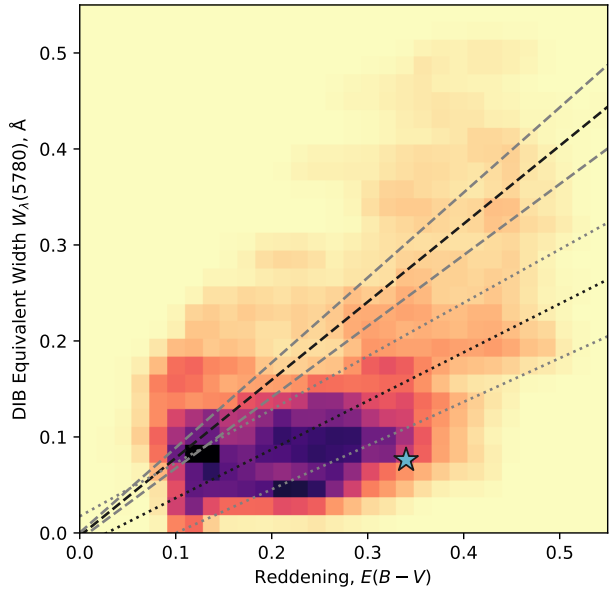


Figure 8. Correlation between DIB equivalent width, $W_\lambda^{\text{obs}}(5780)$, and reddening, $E(B - V)$. False-color image shows histogram of pixels across the face of the nebula, calculated from the MUSE spectral cube: Fig. 6 panel c (y axis) and panel f (x axis), assuming $E(B - V) = 0.3845 \text{ C(H}\beta\text{)}$. Straight lines shows fits to surveys of DIBs along σ -type sight lines to stars (dotted line, Kos & Zwitter 2013) and high-Galactic-latitude sight lines to external galaxies (dashed line, Baron et al. 2015). Star symbol shows result for θ^1 Ori C (Friedman et al. 2011).

3 HIGH-RESOLUTION SPECTROSCOPY OF RAMAN-SCATTERED O I 1028 Å

In order to obtain observations of the Raman-scattered O I absorption lines at high spectral resolution, I have searched through archival spectra of the Orion Nebula obtained with the HIRES spectrograph on the Keck I telescope (Vogt et al. 1994). The observations, obtained in 1997 December 5 and 6, were targeted at a small number of proplyds and jets in the nebula and are described in detail in Henney & O'Dell (1999) and Bally et al. (2000). Unfortunately, the stronger 6633 Å feature falls in a gap between adjacent spectrograph orders and so was not observed. However, the weaker 6664 Å feature falls in order 53 and is detected in many of the spectra. Results for the proplyds will be presented elsewhere, and I concentrate here on 16 slit positions located in the Orion South region, roughly 30 arcsec SW of the Trapezium. Closely similar slit positions are co-added to improve S/N, forming five groups, A to E, with positions shown in Figure 9. Most of the slits are 28 arcsec long and 0.574 arcsec wide, but only the central 11 arcsec of order 53 is usable for faint lines due to overlap of adjacent orders.⁵

The broad Raman-scattered wings to H α are spread over several spectrograph orders and uncertainties in the flat-field correction means that it is impossible to separate the wings from the nebular continuum. Therefore, I simply fit a 5th-order polynomial to line-free sections of the spectrum over the entire order (6649 Å to 6747 Å) and divide to give a continuum-normalized spectrum. Results for the four groups are shown in Figure 10 for the wavelength

⁵ One slit in Group A is 14 arcsec long and does not suffer any order overlap.

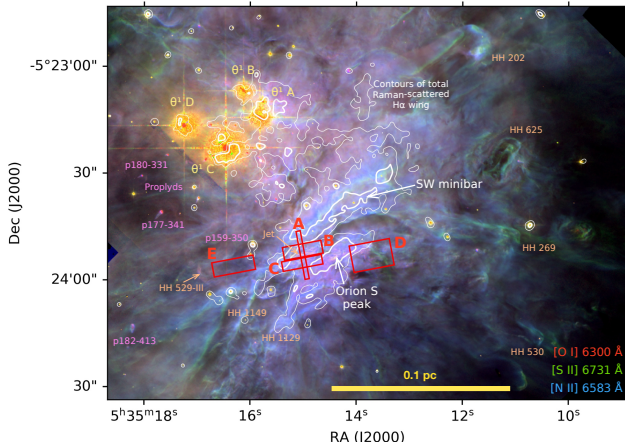


Figure 9. Zoom on Trapezium and Orion South region, showing the locations of extracted Keck spectra (red boxes). The background color composite image shows *HST* WFPC2 observations in the filters F631N, F673N, and F658N (Bally et al. 2000), which highlight emission from the ionization front and adjacent regions. White contours show the total Raman-scattered $H\alpha$ wing emission (sum of the six wavelength bands listed in Table 1).

Table 3. Parameters from single-Gaussian line fits to Keck HIRES spectra

Region	Relative amplitude, A	V , km s^{-1}	W , km s^{-1}
(1)	(2)	(3)	(4)
[Ni II] emission 6666.80 Å			
A	0.75 ± 0.02	0.4 ± 0.1	7.7 ± 0.4
B	0.71 ± 0.02	2.7 ± 0.1	7.9 ± 0.4
C	0.60 ± 0.02	2.9 ± 0.2	8.6 ± 0.5
D	0.46 ± 0.01	1.8 ± 0.2	8.5 ± 0.4
E	0.29 ± 0.01	3.6 ± 0.2	6.8 ± 0.6
O I Raman-scattered absorption 6663.75 Å			
A	0.050 ± 0.003	0.3 ± 0.4	14.5 ± 1.0
B	0.039 ± 0.004	-1.6 ± 0.5	9.6 ± 1.1
C	0.030 ± 0.005	-1.2 ± 0.6	7.6 ± 1.5
D	0.022 ± 0.007	1.3 ± 1.0	7.2 ± 2.5

COLUMNS: (1) Region of nebula covered by HIRES slits (see Figure 9). (2) Peak emission height or absorption depth relative to continuum. (3) Centroid velocity in frame of molecular cloud. (4) Intrinsic full-width half-maximum line width, after correction for the instrumental width of 6 km s^{-1} . Note that in the case of the O I Raman-scattered absorption line the centroid velocity and line widths have been divided by 6.4 to account for the stretching of the Doppler scale between the UV and optical frames.

range of interest. A shallow broad absorption feature is clearly seen around 6664 Å in regions A, B, and C, and arguably in region D, while no such feature is seen in region E. At this high spectral resolution (resolving power $R \approx 50\,000$), the absorption line is well-separated from the adjacent [Ni II] emission line at 6666.8 Å . From Figure 9 it can be seen that regions A, B, and C overlap with contours of strong $H\alpha$ wing emission in the SW minibar, while region E lies in a higher ionization part of the nebula, where the $H\alpha$ wing is weak. This is consistent with the observed relative absorption depths, assuming that the 6664 Å feature is due to Raman scattering of the O I $1028.157\,29$ line (see Table A1).

Table 3 shows results for each slit from fitting both the O I absorption line and the [Ni II] emission line. A single Gaussian component is used for each line and the fits are performed with the

`astropy.modeling` package.⁶ The O I ultraviolet rest wavelength and its optical counterpart after Raman scattering are discussed in Appendix A, while the [Ni II] rest wavelength comes from hollow cathode tube observations Shenstone (1970). Velocities are given in the reference frame of molecular gas in the Orion South region, as defined by the centroid of ^{13}CO emission (Kong et al. 2018): $V_{\text{LSR}} = (+9.0 \pm 0.2) \text{ km s}^{-1}$ or $V_{\odot} = (+28.1 \pm 0.2) \text{ km s}^{-1}$. Both the emission and absorption lines have velocities that are close to that of the molecular gas, as has been previously found for low-ionization lines in the nebula (e.g., Fig. 14 of Baldwin et al. 2000).⁷

The line width is of order 8 km s^{-1} for [Ni II], which is predominantly non-thermal since the thermal broadening is only 3 km s^{-1} for $T = 10^4 \text{ K}$. Compared with other optical emission lines that form near the ionization front, the [Ni II] width is intermediate between the widths of fluorescent lines (e.g., [N I]: $(6 \pm 3) \text{ km s}^{-1}$ Ferland et al. 2012) and collisionally excited lines (e.g., [O I]: $(11.5 \pm 2.6) \text{ km s}^{-1}$ García-Díaz et al. 2008). The Raman-scattered O I line shows the greatest width ($W \approx 15 \text{ km s}^{-1}$) in region A, which is where the absorption is strongest, but is significantly narrower ($W = 7$ to 10 km s^{-1}) in the other regions.

In principle, the kinematics of Raman-scattered lines should be measurable to a higher precision than that of regular lines. This is because the stretching of the Doppler scale means that the effective spectrograph resolving power is multiplied by 6.4 to become $R' = 320\,000$. However, as can be seen from Table 3, the precision of the centroid velocity and width measurements is actually *lower* for O I than for [Ni II].⁸ This is entirely due of the lower signal-to-noise of the absorption line measurements. Therefore, much longer total exposure times than the $4 \times 300 \text{ s}$ of the slits that contribute to region A would be necessary to take full advantage of the boost in spectral resolution provided by Raman scattering.

4 DISCUSSION

In this section, I provide a provisional interpretation of the observational evidence from sections 2 and 3 in the light of simple heuristic models of Raman scattering, such as is illustrated schematically in Figure 11. In section 4.1 I present some formal results from radiative transfer theory that will be used in the following discussion. Section 4.2 investigates how the spatial and spectral characteristics of the broad $H\alpha$ wings can be used to diagnose the physical conditions in the PDR. Section 4.3 considers what extra information can be obtained from the narrow absorption features that are superimposed on the Raman-scattered wings.

4.1 Raman radiative transfer

The Raman scattering process can be divided conceptually into three steps. In step 1, radiative transfer in the FUV band determines the FUV mean intensity, $J_\lambda(\lambda_1)$, at some point in the nebula. In step 2,

⁶ <http://docs.astropy.org/en/stable/modeling/>

⁷ Although the [Ni II] line, which likely arises near the ionization front, seems to show a consistent redshift of order 2 km s^{-1} with respect to CO, this is probably not significant given that the rest wavelength accuracy of 0.03 Å corresponds to 1.4 km s^{-1} .

⁸ The uncertainties are estimated from the parameter covariance array returned by `astropy.modeling.fitting.LevMarLSQFitter`, which uses a least-squares Levenberg-Marquardt algorithm implemented in `scipy.optimize.leastsq` (Virtanen et al. 2020), which in turn is based on the `lmdif` and `lmder` routines in the MINPACK library (Moré 1978).

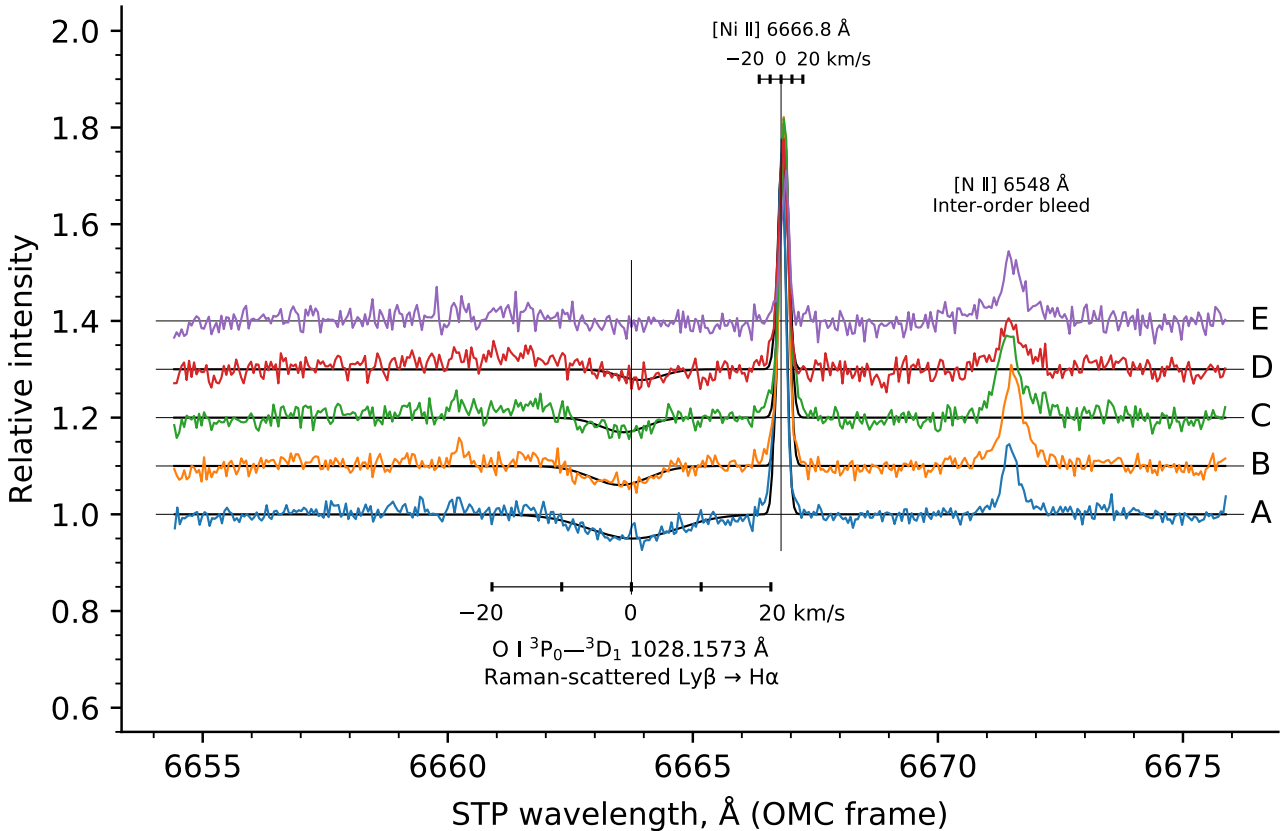


Figure 10. Continuum-normalized Keck HIRES spectra of Raman-scattered O I absorption line for five regions in Orion South. Spectra are offset vertically for ease of comparison. The location of each region is given in Figure 9. Wavelengths are given on an air scale and in the rest-frame of the Orion Molecular Cloud, as defined by the peak velocity of ^{13}CO . Black continuous lines show single-Gaussian fits to the O I absorption line and adjacent [Ni II] emission line, with fit parameters given in Table 3.

the scattering itself (see Appendix A) determines a visual-band emission coefficient $j_\lambda(\lambda_2)$ that is proportional to $J_\lambda(\lambda_1)$, where the visual wavelength, λ_2 , and FUV wavelength, λ_1 , are related by equation (A2). In step 3, radiative transfer in the visual band determines the observed intensity of the H α wing, $I_\lambda(\lambda_2)$. I now consider each of these in turn.

If the FUV radiation field at a point is dominated by a single star of luminosity $L_\lambda^*(\lambda_1)$ at a distance R , then for step 1 we may write

$$4\pi J_\lambda(\lambda_1) = \frac{L_\lambda^*(\lambda_1)}{4\pi R^2} e^{-\tau_1} \quad \text{erg s}^{-1} \text{cm}^{-2} \text{\AA}^{-1} \quad (3)$$

where τ_1 is the FUV optical depth between the point and the star:

$$\tau_1 = \int_0^R k_{\text{total}}(\lambda_1) dR'. \quad (4)$$

The total FUV extinction coefficient can be written as a sum over all absorbing species:

$$k_{\text{total}}(\lambda_1) = \sum_i n_i \sigma_i(\lambda_1) \quad \text{cm}^{-1} \quad (5)$$

Potentially important broad-band absorbers are dust grains and the H 0 Rayleigh/Raman scattering itself. Resonance lines of ions, atoms, and molecules may also be important over narrow ranges of λ_1 . More realistically, one would sum over several equations like

equation (3) for the different stars, and also include the diffuse field due to recombinations, Rayleigh scattering, and dust scattering.

For step 2, assuming that the scattering is isotropic,⁹ the visual-band emission coefficient is simply

$$j_\lambda(\lambda_2) = \left(\frac{\lambda_1}{\lambda_2} \right)^3 J_\lambda(\lambda_1) n(H^0) \sigma(\lambda_1) f_{H\alpha}(\lambda_1) \quad \text{erg s}^{-1} \text{cm}^{-3} \text{sr}^{-1} \text{\AA}^{-1}, \quad (6)$$

where $n(H^0)$ is the number density of neutral hydrogen atoms, $\sigma(\lambda_1)$ is the Rayleigh scattering cross section in the Ly β wing given by equation (A5), and $f_{H\alpha}$ is the branching ratio for Raman conversion given by equation (A6). The factor $(\lambda_1/\lambda_2)^3$ includes one power of λ_1/λ_2 to account for the reduction in energy per photon when passing from the FUV to visual bands, plus two powers of λ_1/λ_2 to account for the transformation of per-angstrom, $d/d\lambda_1 \rightarrow d/d\lambda_2$.

For step 3, the observable intensity, as shown in Figures 4ab and 5a, is given by an integral over all scattering points z along the

⁹ In reality, the scattering is not quite isotropic, but follows the Rayleigh scattering phase function: $\frac{3}{4}(1 + \cos^2 \theta_{\text{scat}})$, where θ_{scat} is the angle between incident and scattered directions. However, this differs from the isotropic case by 50% or less, so equation (6) is a reasonable approximation.

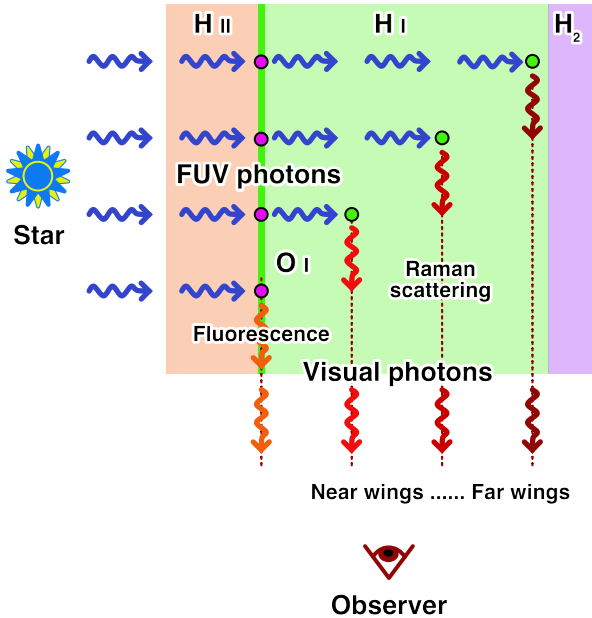


Figure 11. Simplified schematic of where Raman scattering occurs in a PDR. Stellar far-ultraviolet photons (blue wavy arrows) that are far-removed in wavelength from resonant H I lines can pass through the photoionized H II layer relatively unscathed. Some of them will be absorbed by metal resonance lines, such as O I (magenta circles) close to the ionization front, and fluorescently converted to visual/IR photons (orange wavy arrows). This produces a spectral imprint of the O I absorption on the FUV photons that propagate into the PDR. Once the FUV photons have traversed a sufficient column, they will be non-resonantly scattered by H I (green circles) and a significant fraction will be Raman-converted to visual photons (red wavy arrows). For wavelengths farther from line center, this Raman scattering occurs deeper in the PDR and is eventually limited by competition from dust absorption and/or the finite total H I column.

line of sight (los):

$$I_\lambda(\lambda_2) = \int_{\text{los}} j_\lambda(\lambda_2) e^{-\tau_2(z)} dz \quad \text{erg s}^{-1} \text{cm}^{-2} \text{sr}^{-1} \text{\AA}^{-1}, \quad (7)$$

where τ_2 is the visual-band optical depth between each point z and the observer:

$$\tau_2(z) = \int_0^z k_{\text{total}}(\lambda_2) dz' \quad (8)$$

Similarly to the FUV case, the visual-band extinction coefficient $k_{\text{total}}(\lambda_2)$ can be written as a sum over absorbing species, but the only significant absorber in this case is dust.

4.2 Broad-band Raman scattering

An important question to answer with the Raman scattering is whether it is optically thick or optically thin. There are two optical paths to consider (see previous section): the pre-scattered τ_1 of the FUV photons and the post-scattered τ_2 of the visual-band photons. Of these, it is τ_1 that is most interesting since it is affected not only by dust extinction, but also by the opacity of the Rayleigh/Raman scattering itself. The cross section of the Ly β wings varies by more than an order of magnitude between the different Raman bands (column 6 of Table 1), so it is possible that the nearer wings may be optically thick, while the farther wings are optically thin.

4.2.1 Optically thin limit

For the totally optically thin case, $\tau_1, \tau_2 \ll 1$, equations (3, 6, and 7) can be combined to yield

$$I_\lambda(\lambda_2) \approx \left(\frac{\lambda_1}{\lambda_2} \right)^3 \sigma(\lambda_1) f_{H\alpha}(\lambda_1) \frac{L_\lambda^*(\lambda_1)}{16\pi^2} \int_{\text{los}} \frac{n(H^0)}{R^2} dz \quad \text{erg s}^{-1} \text{cm}^{-2} \text{sr}^{-1} \text{\AA}^{-1}. \quad (9)$$

When considering the ratio of Raman-scattered intensities between two different wavelengths for the same position on the nebula, then the line-of-sight integral cancels and one finds

$$\frac{I_\lambda(\lambda_2)}{\sigma(\lambda_1) f_{H\alpha}(\lambda_1)} \propto L_\lambda^*(\lambda_1). \quad (10)$$

The left-hand side of this equation (approximately $(\Delta\lambda_2)^2 I_\lambda(\lambda_2)$) is plotted in Figure 12 for the same extraction regions as in Figure 3. For parts of the spectrum where the scattering is optically thin, this should be proportional to the incident FUV spectrum, $L_\lambda^*(\lambda_1)$, which is dominated by the Trapezium OB stars. It can be seen that the red wing of this compensated spectrum shows an approximately flat section between +80 and +150 Å from H α , covering the R087 and R136 Raman bands. This is consistent with optically thin scattering of a flat FUV spectrum at these wavelengths. However, the same is not seen in the blue wing, where the compensated spectrum continues rising away from line center. It is not at all clear why this is the case, since in nearly all other respects the red and blue wings are remarkably symmetrical (e.g., compare panels a and b of Figure 4). Although the blue wing is certainly more contaminated by weak telluric and nebular lines, this does not seem to be sufficient to explain the discrepancy, which can also be seen in Figure 3 as a broad “shoulder” in the blue wing, extending from 6300 to 6500 Å. One possibility is that the quadratic function used for continuum interpolation is insufficiently accurate, leading to a systematic overestimate of the strength of the blue wing. This might be a result of intermediate scale structure in the dust extinction law (Whiteoak 1966), which has recently been shown to include a broad (≈ 1000 Å) feature centered at 6300 Å (Massa et al. 2020).

Closer to the line center, the results from the two wings are more consistent, with both showing a reduction in compensated intensity. This could mean one of two things: either the Raman wings become optically thick for $|\Delta\lambda_2| < 70$ Å, or the incident FUV spectrum is no longer flat for $|\Delta\lambda_1| < 1.7$ Å, which might correspond to the photospheric Ly β absorption line profile in the spectra of the Trapezium stars.

4.2.2 Optically thick limit

An independent way of discriminating between optically thick and thin scattering is to look at the spatial distribution of the Raman-scattered intensity. In the optically thin limit, this will simply track the spatial distribution of scatterers and so should not vary between the Raman bands. In the optically thick limit, on the other hand, the scattered light will typically arise at $\tau_1 \approx 1$, as I will now demonstrate.

Consider a simplified plane-parallel geometry, as depicted in Figure 11. The FUV photons (blue wavy lines) propagate horizontally, with τ_1 increasing towards the right. The visual photons propagate vertically (red wavy lines), but I assume here that either τ_2 is small or it is independent of λ_2 , in which case it will have no differential effect between the Raman bands. If τ_1 is dominated by the Ly β wing opacity and the total column density of H 0 is sufficiently large, then from equation (3) the mean value of τ_1 weighted

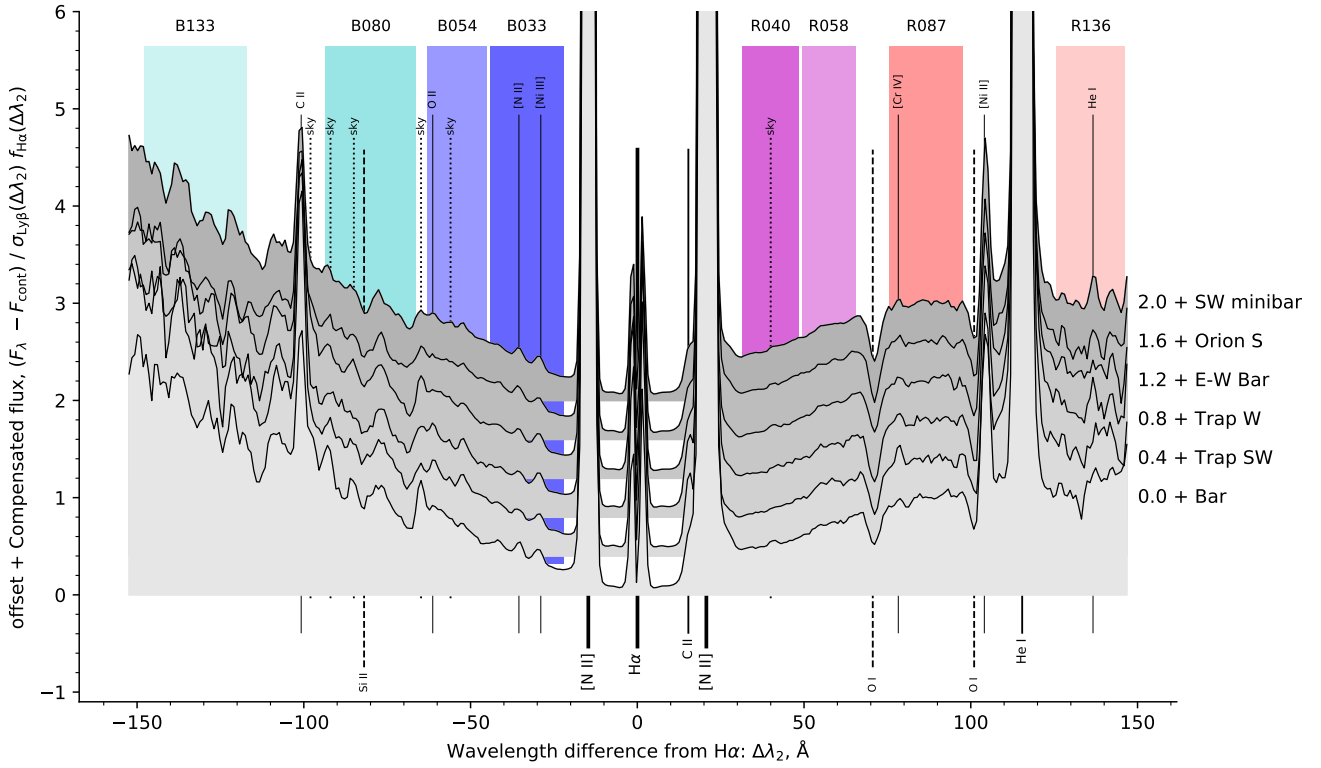


Figure 12. Same as Fig. 3 but with F_λ divided by the effective cross section to Raman scattering $\sigma f_{H\alpha}$ (see Appendix A) and zoomed in on the Raman wing wavelengths. The spectrum is normalized by the average flux in the R087 band and each region is offset vertically by a constant value, as indicated at right. In this presentation, optically thin Raman scattering of a flat FUV spectrum should give a constant value, which for the Orion data is only seen in the R087 and R136 bands.

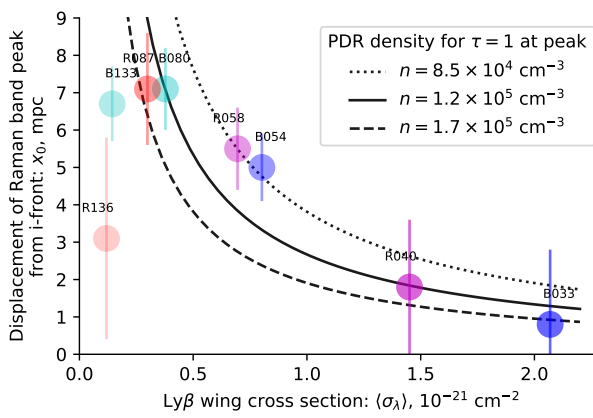


Figure 13. Displacement from the ionization front of the emission peak in each Raman band (column 3 of Table 2), plotted as a function of the cross-section of the Ly β wing (column 6 of Table 1). Color scheme is as in Fig. 3 with error bars showing 10% of the peak FWHM (column 4 of Table 2). Black lines show a simple model in which the peaks occur at $\tau = 1$ for 3 different constant neutral hydrogen densities, as indicated in the legend.

by the FUV mean intensity is

$$|\tau_1| = \frac{\int_0^\infty \tau_1 e^{-\tau_1} d\tau_1}{\int_0^\infty e^{-\tau_1} d\tau_1} = 1, \quad (11)$$

where it is also assumed that R does not vary significantly with τ_1 . If, in addition, $n(H^0)$ and the line-of-sight path length are roughly constant, then from equations (6, 7) the mean τ_1 weighted by the observed intensity $I_\lambda(\lambda_2)$ is also $|\tau_1| \approx 1$.

4.2.3 Raman scattering as a diagnostic of the neutral hydrogen density in the shallow PDR

Based on the results of the previous section, one would expect that the peak Raman emission should occur for a Ly β wing optical depth of $\tau_1 \approx 1$ for each band if the scattering is optically thick. Disregarding dust opacity for the time being, this corresponds to a displacement from the ionization front that varies as $x_0 \approx (n(H^0)\langle\sigma_\lambda\rangle)^{-1}$, where $n(H^0)$ is the neutral hydrogen density in the PDR and $\langle\sigma_\lambda\rangle$ is the Ly β wing cross section for the FUV wavelengths that pump each band, which is given in column 6 of Table 1. In Figure 13, this relationship is compared with the measurements of the Orion Bar given in section 2.5. under the assumption that $n(H^0)$ is constant over the depth range 2 mpc to 8 mpc. It can be seen that a PDR density of order $n(H^0) \sim 10^5 \text{ cm}^{-3}$ provides a good fit to the observations for bands within about 100 Å of line center. A systematic uncertainty of 10% of the width of each emission peak is assigned to the x_0 values, which has the largest relative impact on the near-wing bands: B033 and R040. As a result, it is the B054 and R058 bands that are the most reliable indicators, yielding $n(H^0) = 8.5 \times 10^4 \text{ cm}^{-3}$ (dotted line). The bands in the farther wings fall below this curve, significantly so for B133 and R136, but this can be understood as

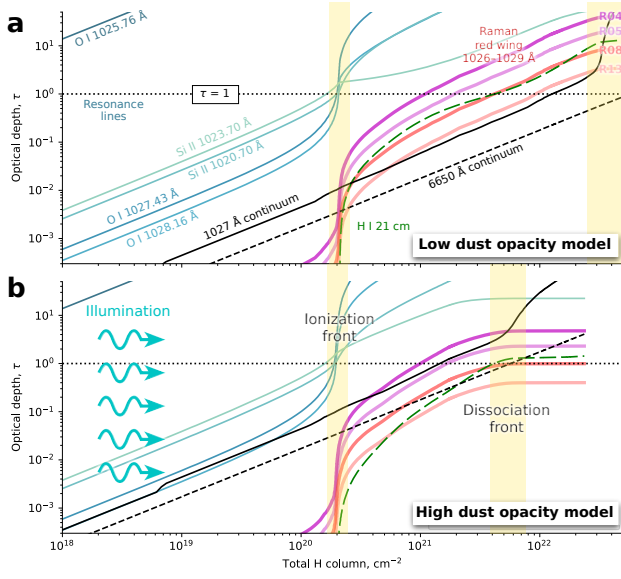


Figure 14. Optical depth of select processes as a function of total hydrogen nucleon column density, calculated from static Cloudy simulations of the Orion Bar. All optical depths and columns are measured with respect to the illuminating Trapezium stars, which are situated to the left in this figure. Separate panels show two models that differ only in the assumed dust absorption opacity: (a) low opacity, $\sigma_{\text{FUV}} \approx 5 \times 10^{-23} \text{ cm}^2 \text{ H}^{-1}$, and (b) high opacity, $\sigma_{\text{FUV}} \approx 5 \times 10^{-22} \text{ cm}^2 \text{ H}^{-1}$. Optical depths of O⁰ and Si⁺ absorption lines in the Ly β wings are shown in blue. Continuum optical depths near Ly β (solid line) and H α (dashed line) are shown in black. The H⁰ 21 cm line optical depth is shown in green (long dashed line). Optical depths to Rayleigh/Raman scattering for 4 observed bands in the red wing of Ly β (see Table 1) are shown in red.

due to two factors. First, the finite total H⁰ column through the PDR means that the wings will become optically thin for a sufficiently low $\langle \sigma_\lambda \rangle$, in which case $\tau = 1$ can no longer hold. Second, competition with dust grains for the absorption of FUV photons will become significant when $\langle \sigma_\lambda \rangle < \sigma_{\text{dust}}$.

4.2.4 Cloudy model predictions for the optical depths

4.3 Absorption features in the Raman pseudo-continuum

In lieu of solving the full radiative transfer equation, I assume that the Rayleigh and Raman-scattering occurs in a region where the FUV optical depth from the illuminating star is $\tau \approx 1$ in the Ly β wing. I ignore the possibility of multiple Rayleigh scattering before Raman conversion. I also disregard dust extinction of the post-scattered visual-band photons, although the effects of FUV dust opacity are more important and are considered below.

Location of H⁰. Neutral veil in front of nebula has column density of $1.6 \times 10^{21} \text{ cm}^{-2}$ and $3.2 \times 10^{21} \text{ cm}^{-2}$ in components A and B (Abel et al. 2006).

4.4 Evidence for Raman-scattered absorption lines

4.5 Structure of the Orion Bar

Geometry of bar: in Henney et al. (2005) I pointed out that a diverging cylindrical geometry is necessary to explain the sharp peak in the [N II] emissivity seen at the ionization front. It has been apparent

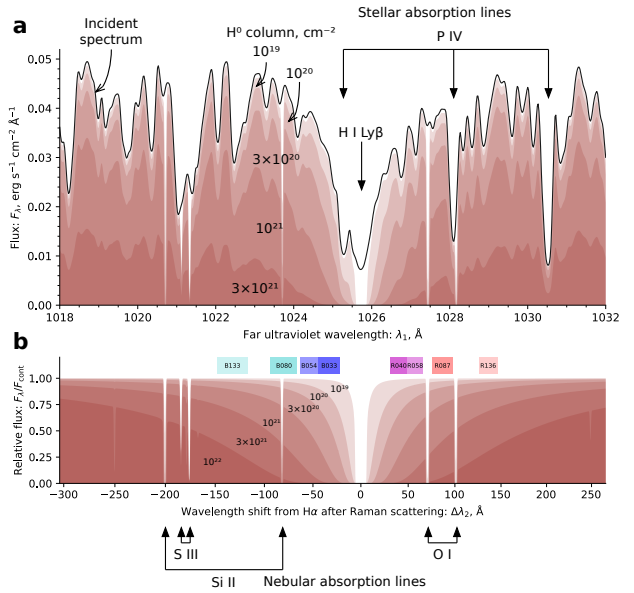


Figure 15. (a) Predicted spectrum of Trapezium stars in vicinity of Ly β from POWR OB atmosphere models (black line), together with attenuation by Cloudy model of the Orion Bar (red filled shapes), extracted at a series of values of the neutral hydrogen column density, as marked. (b) Relative attenuation of the incident spectrum by line opacity only (that is, neglecting dust continuum opacity) in the Cloudy models, which shows the development of the Ly β damping wings as the column density increases. In this panel, the x axis is labelled with $\Delta\lambda_2$ in the optical domain, allowing direct comparison with the observations presented in Figure 12 (observed Raman bands are indicated by colored boxes). Note that the scale is linear in λ_1 , which is slightly non-linear in $\Delta\lambda_2$. Wavelengths of some of the more prominent stellar photospheric lines and nebular absorption lines are marked.

since O'Dell & Yusef-Zadeh (2000) that the nebula contains many bar-like features.

Salgado et al. (2016) had found low dust cross-section in Orion Bar PDR, but there are loopholes. First, they assume plane-parallel geometry with exactly edge-on viewing angle, while in reality it is a roughly cylindrical filament. Second, they ignore scattering, see Watson et al. (1998). Also, density increase with depth

4.6 The failure of rival explanations for the 6633, 6664 Å lines

In this paper, I provide a strong case for identifying the absorption features at 6633 and 6664 Å with Raman-scattered FUV O I absorption lines (see Appendix A). However, it is important to thoroughly investigate potential competing explanations, if only to rule them out.

4.6.1 Why they cannot be dust-scattered stellar absorption lines

Various photospheric absorption lines of luminous O stars are visible in the spectrum of the diffuse nebula due to scattering of the starlight by dust grains in the H II region and surrounding PDR. These are clearest in the case of high-ionization lines that are absent from the emission spectrum of the nebular gas, such as the He II and C IV lines that were analysed above in § 2.6.2. At first glance, it might seem that the equivalent width map of the 6633 Å feature (Figure 6a) is similar to that of the C IV absorption lines (Figure 6e).

However, there are important differences: the ridge of peak C IV absorption lies at about 20 to 30 arcsec from the Trapezium stars, close to the “Trap SW” region shown in Figure 2b, whereas the 6633 Å absorption ridges lie farther from the Trapezium (50 to 60 arcsec) in the “SW minibar” and “Orion S” regions. This implies that the spatial distribution of scatterers is different between the two cases. This is exactly what would be expected under the Raman-scattering hypothesis for 6633 Å, since the scatterers are neutral hydrogen atoms, located in the PDR outside the H II region, whereas the stellar continuum is scattered by dust grains, some of which will be inside the H II region.¹⁰

An even stronger argument against a visual-band stellar origin is that no absorption features at 6633 or 6664 Å are seen in the luminous OB stars of the nebula. The closest match is a pair of Fe I features at 6634 and 6664 Å, which are seen in absorption in the photospheres of several K and M-type T Tauri stars in the Orion Nebula cluster. One of the brightest and most centrally located examples is V2279 Ori (Parenago 1869, JW 499, TCC 52), a visual binary (spectral type M0.5 + M2; Daemgen et al. 2012) which is the central star of the prominent proplyd 159-350 (HST 3; O’Dell et al. 1993). However, the luminosity of this source is only $\approx 10 L_\odot$ and its brightness around 6650 Å is 200 times smaller than that of θ^1 Ori C. Furthermore, photospheric lines are weak in T Tauri stars due to accretion veiling and the equivalent widths of these absorption features are only $W_\lambda^\star \approx 0.1$ Å. Therefore, even several such stars would contribute at most 0.001 Å to the equivalent width in the diffuse nebular spectrum, which is far less than the observed values of up to $W_\lambda^{\text{obs}} = 0.5$ Å (Figure 6a).

4.6.2 Why they cannot be visual-band neutral/molecular absorption lines from the PDR

The fact that the 6633 and 6664 Å features are not seen in the spectra of the luminous stars, such as θ^1 Ori C, means that they cannot arise in the foreground neutral gas of the Orion veil (Abel et al. 2004, 2019). However, if some neutral or molecular species were abundant in the dense PDR behind the nebula, but *not* in the Veil, then it is theoretically possible that it might imprint an absorption signature on the starlight that initially enters the PDR but is then reflected out again by dust scattering. On the other hand, such a scenario seems very far-fetched and I have been unable to find any candidate absorption features at relevant wavelengths.

4.6.3 Why they cannot be solid-state absorption features

The same argument as in the previous section also rules out any possibility that foreground DIB absorption might be responsible for these features, with the additional argument that the 6633 Å equivalent width does not correlate with foreground extinction, as the known DIB at 5780 Å does. However, that leaves open the possibility of the contrived back-scattering scenario discussed above. There is a DIB at 6632.85 Å (Galazutdinov et al. 2000), which is consistent in wavelength with the 6633 Å feature but it is only seen in highly-reddened stars and is always at least 10 times weaker than

¹⁰ One piece of evidence for the presence of dust inside the H II region is that the gas-phase abundances of nickel and iron are seen to be enhanced in photoionized Herbig-Haro outflows within the nebula (Mesa-Delgado et al. 2009), consistent with dust destruction in shocks. Indirect evidence also comes from the dust-scattered redshifted wing of nebular emission lines (Henney 1998).

the 5780 Å feature. From Figure 8 it is conceivable that up to half of the 5780 Å absorption might arise during back-scattering from the PDR rather than in foreground material for some sight lines. This would imply an equivalent width $W_\lambda < 0.02$ Å for the 6632.85 Å DIB, which is much smaller than the observed $W_\lambda^{\text{obs}}(6633) \approx 0.5$ Å (Figure 6a).

4.7 What high-resolution spectra tell us

The observed width of the Raman-scattered O I line (§ 3) can be used to derive an upper limit to the gas temperature in the scattering region via the following argument. In addition to the thermal and non-thermal (turbulent) broadening of the O I absorption line itself, the Raman-scattered line will be further broadened by motions of the H⁰ scatterers. Part of this broadening will be due to velocity gradients between the line formation region and the scattering region. However, the close agreement in centroid velocity (< 2 km s⁻¹) between atomic fluorescent lines and CO lines (Baldwin et al. 2000) implies that any such gradients are small. The other part will be due to thermal motions of the scatterers, which will contribute a width (FWHM) of

$$\Delta V_{\text{therm}} = 0.124(T/A)^{1/2} \text{ km s}^{-1}, \quad (12)$$

where T is the temperature in K and A is the standard relative atomic mass. Measured widths of optical O I fluorescent lines are relatively large (> 10 km s⁻¹, Baldwin et al. 2000) but this is due to the presence of multiple fine-structure components, with splittings of a few km s⁻¹, and so they do not help constrain the Doppler width of the UV O I 1028 Å line. Instead we use the 6 km s⁻¹ width of the [N I] 5200 Å line (Ferland et al. 2012), which is also fluorescently excited and is unaffected by fine-structure broadening. The most stringent limit on the temperature is given by the smallest observed width of the 6664 Å feature, for which we take the region C value of 7.6 km s⁻¹ (Table 3).¹¹ Subtracting 6 km s⁻¹ in quadrature and substituting into equation (12) yields an upper limit of $T \leq 480$ K for the Raman-scattering region.

This is further evidence that Raman scattering by H⁰ must be occurring in the fully-neutral PDR, rather than the partially ionized ionization front, where the temperature is of order 10⁴ K. It is interesting to contrast the Raman-scattered lines with the case of the deuterium Balmer lines, which are also believed to be excited by fluorescence (Hébrard et al. 2000; O’Dell et al. 2001). The minimum width of these lines is observed to be 9 km s⁻¹, which from equation (12) with $A = 2$ yields $T = 10500$ K if the broadening is purely thermal, or $T = 6000$ K assuming non-thermal broadening of 6 km s⁻¹. Either case is consistent with the deuterium lines being formed in the ionization front itself. The difference with the Raman scattering can be explained by the magnitudes of the relevant cross sections. A typical resonance line that excites the deuterium Balmer lines is deuterium Lyman γ , which, assuming D/H = 1.5×10^{-5} , has cross section of $\approx 4 \times 10^{-20} \text{ cm}^2 (\text{H}^0)^{-1}$. This is considerably larger than the Raman wing cross section at 1028 Å, which is only $\approx 2 \times 10^{-22} \text{ cm}^2 (\text{H}^0)^{-1}$ (see Table 1 and Appendix A).

4.8 Miscellany

The effective resolving power of the optical spectrograph is multiplied by 6.4 for the FUV domain.

¹¹ Although the region D value is smaller, the signal-to-noise is too small for it to be reliable.

The O I lines should be in absorption in the spectrum seen by the Raman scatterers.

Non-equilibrium PDRs (Stoerzer & Hollenbach 1998; Bertoldi & Draine 1996). Recent models from Bron et al. (2018).

C I emission from non-steady PDRs (Stoerzer et al. 1997) (fine structure lines, but maybe optical lines would be similar). Escalante et al. (1991) model the far-red [C I] line as recombination of C⁺.

O VI 1037.62, 1031.93 absorption line in wind. No evidence for a blue absorption edge at $V = 1200 \text{ km s}^{-1}$, which would be at $\lambda_2 = 6649 \text{ \AA}$, right in middle of R087 band.

Even for high PDR optical depth, no multiple Raman scattering will occur since the population of 2s is very small and the post-scattered photons have insufficient energy to excite any transitions from 1s.

5 CONCLUSIONS

From the spatial distribution of the He II 4686 Å absorption line in dust-scattered light, we find further evidence that θ¹ Ori D is situated behind the other Trapezium stars, closer to the background cloud, as was originally suggested by (Smith et al. 2005).

ACKNOWLEDGEMENTS

I am grateful for financial support provided by Dirección General de Asuntos del Personal Académico, Universidad Nacional Autónoma de México, through grant Programa de Apoyo a Proyectos de Investigación e Innovación Tecnológica IN107019. Scientific software and databases used in this work include SAOImage DS9¹² (Joye & Mandel 2003), the Atomic Line List¹³ (Van Hoof 2018), the Cloudy plasma physics code¹⁴ (Ferland et al. 2017), SIMBAD and Vizier from Strasbourg Astronomical Data Center (CDS)¹⁵, and the following 3rd-party Python packages: numpy, astropy, matplotlib, seaborn, scikit-image, reproject.

DATA AVAILABILITY

The primary data underlying this article are two spectroscopic datasets. First, integral field spectral mosaics of the inner Orion Nebula, obtained with the MUSE spectrograph on the VLT, which are available from <http://muse-vlt.eu/science/m42/>. Second, longslit spectra of the Orion S region, obtained with the HIRES spectrograph on the Keck I telescope, which are available from the Keck Observatory Archive at <https://koa.ipac.caltech.edu/cgi-bin/KOA/nph-KOALogin>. Additional supporting data from other observatories and archives may be accessed via the references given in the main text. All data reduction and analysis programs used in this paper, together with documentation and research notes may be found at <https://github.com/will-henney/dib-scatter-hii>.

References

- Abel N. P., Brogan C. L., Ferland G. J., O'Dell C. R., Shaw G., Troland T. H., 2004, *ApJ*, **609**, 247
 Abel N. P., Ferland G. J., O'Dell C. R., Shaw G., Troland T. H., 2006, *ApJ*, **644**, 344
 Abel N. P., Ferland G. J., O'Dell C. R., 2019, arXiv e-prints, p. arXiv:1906.07779
 Arab H., Abergel A., Habart E., Bernard-Salas J., Ayasso H., Dassas K., Martin P. G., White G. J., 2012, *A&A*, **541**, A19
 Bacon R., et al., 2010, in Proc. SPIE. p. 773508, doi:10.1117/12.856027
 Bacon R., et al., 2014, *The Messenger*, **157**, 13
 Baldwin J. A., Verner E. M., Verner D. A., Ferland G. J., Martin P. G., Korista K. T., Rubin R. H., 2000, *ApJS*, **129**, 229
 Bally J., O'Dell C. R., McCaughrean M. J., 2000, *AJ*, **119**, 2919
 Baron D., Poznanski D., Watson D., Yao Y., Prochaska J. X., 2015, *MNRAS*, **447**, 545
 Bernard-Salas J., et al., 2012, *A&A*, **538**, A37
 Bertoldi F., Draine B. T., 1996, *ApJ*, **458**, 222
 Blagrave K. P. M., Martin P. G., Rubin R. H., Dufour R. J., Baldwin J. A., Hester J. J., Walter D. K., 2007, *ApJ*, **655**, 299
 Bregman J. D., Allamandola L. J., Tielens A. G. G. M., Geballe T. R., Witteborn F. C., 1989, *ApJ*, **344**, 791
 Bron E., Agúndez M., Goicoechea J. R., Cernicharo J., 2018, arXiv e-prints, Cesarsky D., Jones A. P., Lequeux J., Verstraete L., 2000, *A&A*, **358**, 708
 Chang S.-J., Heo J.-E., Di Mille F., Angeloni R., Palma T., Lee H.-W., 2015, *ApJ*, **814**, 98
 Clegg R. E. S., Miller S., Storey P. J., Kisielius R., 1999, *A&AS*, **135**, 359
 Conti P. S., 1972, *ApJ*, **174**, L79
 Cordiner M. A., et al., 2019, *ApJ*, **875**, L28
 Da Rio N., Robberto M., Soderblom D. R., Panagia N., Hillenbrand L. A., Palla F., Stassun K., 2009, *ApJS*, **183**, 261
 Daemgen S., Correia S., Petr-Gotzens M. G., 2012, *A&A*, **540**, A46
 Desert F.-X., Boulanger F., Puget J. L., 1990, *A&A*, **237**, 215
 Donati J.-F., Babel J., Harries T. J., Howarth I. D., Petit P., Semel M., 2002, *MNRAS*, **333**, 55
 Dopita M. A., Nicholls D. C., Sutherland R. S., Kewley L. J., Groves B. A., 2016, *ApJ*, **824**, L13
 Escalante V., Sternberg A., Dalgarno A., 1991, *ApJ*, **375**, 630
 Ferland G. J., Henney W. J., O'Dell C. R., Porter R. L., van Hoof P. A. M., Williams R. J. R., 2012, *ApJ*, **757**, 79
 Ferland G. J., et al., 2017, *Rev. Mex. Astron. Astrofis.*, **53**, 385
 Friedman S. D., et al., 2011, *ApJ*, **727**, 33
 Galazutdinov G. A., Musaev F. A., Krełowski J., Walker G. A. H., 2000, *PASP*, **112**, 648
 García-Díaz M. T., Henney W. J., 2007, *AJ*, **133**, 952
 García-Díaz M. T., Henney W. J., López J. A., Doi T., 2008, *Rev. Mex. Astron. Astrofis.*, **44**, 181
 García-Díaz M. T., Steffen W., Henney W. J., López J. A., García-López F., González-Buitrago D., Áviles A., 2018, *MNRAS*, **479**, 3909
 Goicoechea J. R., et al., 2017, *A&A*, **601**, L9
 Greisen E. W., Calabretta M. R., Valdes F. G., Allen S. L., 2006, *A&A*, **446**, 747
 Heger M. L., 1922, *Lick Observatory Bulletin*, **10**, 141
 Henney W. J., 1998, *ApJ*, **503**, 760
 Henney W. J., O'Dell C. R., 1999, *AJ*, **118**, 2350
 Henney W. J., Arthur S. J., Williams R. J. R., Ferland G. J., 2005, *ApJ*, **621**, 328
 Hobbs L. M., et al., 2008, *ApJ*, **680**, 1256
 Hébrard G., Péquignot D., Vidal-Madjar A., Walsh J. R., Ferlet R., 2000, *A&A*, **354**, L79
 Ivanov T. I., Salumbides E. J., Vieitez M. O., Cacciani P. C., de Lange C. A., Ubachs W., 2008, *MNRAS*, **389**, L4
 Joye W. A., Mandel E., 2003, in Payne H. E., Jedrzejewski R. I., Hook R. N., eds, *Astronomical Society of the Pacific Conference Series Vol. 295, Astronomical Data Analysis Software and Systems XII*. p. 489
 Kassis M., Adams J. D., Campbell M. F., Deutsch L. K., Hora J. L., Jackson J. M., Tollestrup E. V., 2006, *ApJ*, **637**, 823

¹² <https://sites.google.com/cfa.harvard.edu/saoimageds9>

¹³ <https://www.pa.uky.edu/~peter/newpage/>

¹⁴ <https://nublado.org>

¹⁵ <https://cds.u-strasbg.fr>

- Kissler-Patig M., et al., 2008, *A&A*, **491**, 941
- Kong S., et al., 2018, *ApJS*, **236**, 25
- Kos J., Zwitter T., 2013, *ApJ*, **774**, 72
- Kounkel M., et al., 2017, *ApJ*, **834**, 142
- Krełowski J., Westerlund B. E., 1988, *A&A*, **190**, 339
- Krełowski J., Galazutdinov G., Godunova V., Bondar A., 2019, *Acta Astron.*, **69**, 159
- Lai T. S. Y., Witt A. N., Alvarez C., Cami J., 2020, *MNRAS*, **492**, 5853
- Luhman K. L., Engelbracht C. W., Luhman M. L., 1998, *ApJ*, **499**, 799
- Marconi A., Testi L., Natta A., Walmsley C. M., 1998, *A&A*, **330**, 696
- Marinov D., Booth J. P., Drag C., Blondel C., 2017, *Journal of Physics B Atomic Molecular Physics*, **50**, 065003
- Martin W. C., Zalubas R., 1983, *Journal of Physical and Chemical Reference Data*, **12**, 323
- Massa D., Fitzpatrick E. L., Gordon K. D., 2020, *ApJ*, **891**, 67
- Maíz Apellániz J., et al., 2019, *A&A*, **626**, A20
- McLeod A. F., Weilbacher P. M., Ginsburg A., Dale J. E., Ramsay S., Testi L., 2016, *MNRAS*, **455**, 4057
- Megeath S. T., et al., 2012, *AJ*, **144**, 192
- Mesa-Delgado A., Esteban C., García-Rojas J., Luridiana V., Bautista M., Rodríguez M., López-Martín L., Peimbert M., 2009, *MNRAS*, **395**, 855
- Moehler S., et al., 2014, *A&A*, **568**, A9
- Mohr P. J., Taylor B. N., Newell D. B., 2008, *Rev. Mod. Phys.*, **80**, 633
- More J. J., 1978, in Watson G. A., ed., *Numerical Analysis*. Springer Berlin Heidelberg, Berlin, Heidelberg, pp 105–116
- Noll S., Kausch W., Barden M., Jones A. M., Szyszka C., Kimeswenger S., Vinther J., 2012, *A&A*, **543**, A92
- Noll S., Kausch W., Kimeswenger S., Barden M., Jones A. M., Modigliani A., Szyszka C., Taylor J., 2014, *A&A*, **567**, A25
- Nussbaumer H., Schmid H. M., Vogel M., 1989, *A&A*, **211**, L27
- O'Dell C. R., Yusef-Zadeh F., 2000, *AJ*, **120**, 382
- O'Dell C. R., Wen Z., Hu X., 1993, *ApJ*, **410**, 696
- O'Dell C. R., Ferland G. J., Henney W. J., 2001, *ApJ*, **556**, 203
- O'Dell C. R., Ferland G. J., Peimbert M., 2017, *MNRAS*, **464**, 4835
- Omont A., Bettinger H. F., Tönshoff C., 2019, *A&A*, **625**, A41
- Osterbrock D. E., Ferland G. J., 2006, *Astrophysics of gaseous nebulae and active galactic nuclei*, second edn. Sausalito, CA: University Science Books
- Osterbrock D. E., Fulbright J. P., Martel A. R., Keane M. J., Trager S. C., Basri G., 1996, *PASP*, **108**, 277
- Parikka A., Häbärt E., Bernard-Salas J., Köhler M., Abergel A., 2018, *A&A*, **617**, A77
- Salgado F., Berné O., Adams J. D., Herter T. L., Keller L. D., Tielens A. G. G. M., 2016, *ApJ*, **830**, 118
- Schmid H. M., 1989, *A&A*, **211**, L31
- Shenstone A. G., 1970, *Journal of research of the National Bureau of Standards. Section A, Physics and chemistry*, **74A**, 801
- Simón-Díaz S., Herrero A., Esteban C., Najarro F., 2006, *A&A*, **448**, 351
- Smette A., et al., 2015, *A&A*, **576**, A77
- Smith N., Bally J., Shuping R. Y., Morris M., Kassis M., 2005, *AJ*, **130**, 1763
- Sonnentrucker P., 2014, in Cami J., Cox N. L. J., eds, IAU Symposium Vol. 297, *The Diffuse Interstellar Bands*. pp 13–22, doi:10.1017/S1743921313015524
- Stahl O., Wolf B., Gang T., Gummersbach C. A., Kaufer A., Kovacs J., Mandel H., Szeifert T., 1993, *A&A*, **274**, L29
- Stahl O., et al., 1996, *A&A*, **312**, 539
- Stoerzer H., Hollenbach D., 1998, *ApJ*, **495**, 853
- Stoerzer H., Stutzki J., Sternberg A., 1997, *A&A*, **323**, L13
- Subrahmanyam R., Goss W. M., Malin D. F., 2001, *AJ*, **121**, 399
- Tielens A. G. G. M., 2014, in Cami J., Cox N. L. J., eds, IAU Symposium Vol. 297, *The Diffuse Interstellar Bands*. pp 399–411, doi:10.1017/S1743921313016207
- Van Hoof P. A. M., 2018, *Galaxies*, **6**
- Virtanen P., et al., 2020, *Nature Methods*, **17**, 261
- Vogt S. S., et al., 1994, in Crawford D. L., Craine E. R., eds, *Society of Photo-Optical Instrumentation Engineers (SPIE) Conference Series* Vol. 2198, *Instrumentation in Astronomy VIII*. p. 362, doi:10.1117/12.176725
- Walmsley C. M., Natta A., Oliva E., Testi L., 2000, *A&A*, **364**, 301
- Watson A. M., Henney W. J., Escalante V., 1998, in *American Astronomical Society Meeting Abstracts*. p. 16.03
- Weilbacher P. M., et al., 2015, *A&A*, **582**, A114
- Whiteoak J. B., 1966, *ApJ*, **144**, 305
- ud-Doula A., Sundqvist J. O., Owocki S. P., Petit V., Townsend R. H. D., 2013, *MNRAS*, **428**, 2723
- van der Werf P. P., Stutzki J., Sternberg A., Krabbe A., 1996, *A&A*, **313**, 633

APPENDIX A: RAMAN SCATTERING THEORY

When a photon is Raman-scattered from the vicinity of Ly β (UV domain) to the vicinity of H α (optical domain) its wavelength is transformed from λ_1 to λ_2 . Intervals in frequency ($\nu = c/\lambda$) or wavenumber ($\tilde{\nu} = 1/\lambda$) space are conserved between the two domains. For example the wavenumber displacement from the H 1 line center can be written in two ways:

$$\Delta\tilde{\nu} = \tilde{\nu}_1 - \tilde{\nu}(\text{Ly}\beta) = \tilde{\nu}_2 - \tilde{\nu}(\text{H}\alpha), \quad (\text{A1})$$

from which it follows that

$$\lambda_2 = \left(\frac{1}{\lambda(\text{H}\alpha)} + \frac{1}{\lambda_1} - \frac{1}{\lambda(\text{Ly}\beta)} \right)^{-1}. \quad (\text{A2})$$

The wavelengths $\lambda(\text{Ly}\beta)$ and $\lambda(\text{H}\alpha)$, together with their corresponding wavenumbers, are given in Table A1 (all wavelengths are on the vacuum scale unless otherwise noted). For both lines, a weighted average over the $3p\ ^2P_{1/2}$ and $3p\ ^2P_{3/2}$ upper levels is used, assumed to be populated according to their statistical weights, with individual component wavelengths obtained from Tab. XXVIII of Mohr et al. (2008). Note that the electric dipole selection rules mean that only $3p \rightarrow 2s$ transitions contribute to H α in the Raman scattering context. The wavelength is therefore slightly shorter than the value obtained for the H α recombination line, which includes additional contributions from $3s \rightarrow 2p$ and $3d \rightarrow 2p$. The shift is of order -0.05 \AA or -2 km s^{-1} with respect to the Case B results reported in Tab. 6a of Clegg et al. (1999).

Also listed in Table A1 are the Raman transformations $\lambda_1 \rightarrow \lambda_2$ for the rest wavelengths of transitions between the ground $2s^2 2p^4 \ ^3P$ term of neutral ^{16}O and the excited $2s^2 2p^3 3d\ ^3D^0$ term. The OI data is obtained from highly accurate laser metrology (Ivanov et al. 2008; Marinov et al. 2017), with a precision of 0.08 cm^{-1} or better. The fine structure splitting between the J_k levels of the excited term ($\sim 0.1 \text{ cm}^{-1}$) is much smaller than that between the J_i levels of the ground term ($\sim 100 \text{ cm}^{-2}$), so that the 6 transitions fall into 3 well-separated groups. The three transitions from the lowest energy $J_i = 2$ level are very close to Ly β ($\Delta\tilde{\nu} \approx 4 \text{ cm}^{-1}$), whereas the two transitions from $J_i = 1$ ($\Delta\tilde{\nu} \approx 162 \text{ cm}^{-1}$) and the single transition from $J_i = 0$ ($\Delta\tilde{\nu} \approx 231 \text{ cm}^{-1}$) lie increasingly to the red. The corresponding wavelengths in the optical domain, λ_2 , are therefore on the red side of H α . The final column of the table uses STP refractive indices (Greisen et al. 2006) to convert λ_2 to air wavelengths, λ_{air} , for ease of comparison with ground-based optical spectroscopy. The resultant wavelength is 6663.747 \AA for the line from $J_i = 0$, with an uncertainty of about 0.004 \AA , which is much smaller than typical observational precision (for instance, 0.07 \AA for a very high resolution spectrograph with resolving power of $R = 10^5$). The two lines from $J_i = 1$, with a separation of 0.028 \AA , will always be blended in observations, giving a mean wavelength of 6633.347 \AA (assuming the upper levels are distributed according to statistical weight $2J_k + 1$). Similarly, the three lines from $J_i = 2$ have a mean wavelength of 6564.386 \AA , but this is so close to H α

Table A1. FUV/optical wavelength equivalencies for Raman scattering

Ion	Transition	$J_i \rightarrow J_k$	$\lambda_1, \text{\AA}$	$\tilde{\nu}_1, \text{cm}^{-1}$	$\Delta\tilde{\nu}, \text{cm}^{-1}$	$\tilde{\nu}_2, \text{cm}^{-1}$	$\lambda_2, \text{\AA}$	$\lambda_{\text{air}}, \text{\AA}$
		 Ly β , $n = 1$	H α , $n = 2$
H I	$ns^2 2S \rightarrow 3p^2 2P$	$1/2 \rightarrow 1/2, 3/2$	1025.72220	97492.283	0.000	15233.329	6564.553	6562.740
O I	$2s^2 2p^4 3P \rightarrow 2s^2 2p^3 (4S) 3d^3 D^0$	$0 \rightarrow 1$ $1 \rightarrow 1$ $1 \rightarrow 2$ $2 \rightarrow 1$ $2 \rightarrow 2$ $2 \rightarrow 3$	1028.15729 1027.43139 1027.43077 1025.76339 1025.76276 1025.76170	97261.383 97330.100 97330.159 97488.369 97488.429 97488.530	-230.900 -162.183 -162.124 -3.914 -3.854 -3.753	15002.429 15071.146 15071.205 15229.415 15229.475 15229.576	6665.587 6635.196 6635.170 6633.338 6566.240 6566.171	6663.747 6633.364 6633.338 6564.427 6564.401 6564.358
Si II	$3s^2 3p^2 P^0 \rightarrow 3s^2 5s^2 S$	$1/2 \rightarrow 1/2$ $1/2 \rightarrow 3/2$	1020.6989 1023.7001	97972.086 97684.859	+479.803 192.576	15713.132 15425.905	6364.104 6482.602	6362.345 6480.811

(corresponding to a Doppler shift of $+75 \text{ km s}^{-1}$) that it would be very difficult to observe.

The final section of Table A1 gives data for a resonance doublet of Si $^+$ whose components lie a few Å to the blue of Ly β . The shorter of the two components is Raman-transformed to $\lambda_{\text{air}} = 6362.35 \text{ \AA}$, which unfortunately coincides with the collisionally excited [O I] line at 6363.78 \AA . The longer component is transformed to 6480.81 \AA in a region that is clear of any strong nebular lines. Wavelengths for these lines are based on energy levels from Martin & Zalubas (1983), with an estimated precision of 0.1 cm^{-1} , which gives an uncertainty in the optical wavelengths λ_2 of 0.04 \AA .

The total cross-section for the off-resonance $1s \rightarrow 3p$ transition in H 0 is calculated in § 2 of Chang et al. (2015) from second order time-dependent perturbation theory. Results are presented in the upper panel of Figure 1 of that paper in terms of a Doppler velocity factor ΔV_1 , which in the notation of the current paper is

$$\Delta V_1 = c \left(\frac{\lambda_1}{\lambda(\text{Ly}\beta)} - 1 \right). \quad (\text{A3})$$

The observed Raman-scattered wings of H α that are analyzed in this paper are typically within $\Delta\lambda_2 \sim \pm 100 \text{ \AA}$ of the line core. It is therefore convenient to define a dimensionless wavelength in the optical domain as

$$x = \frac{\lambda_2 - \lambda(\text{H}\alpha)}{100 \text{ \AA}}, \quad (\text{A4})$$

which corresponds to $x \approx \Delta V_1 / 714 \text{ km s}^{-1}$ in the FUV domain. The total cross section in the range $0.4 < |x| < 2.3$ can then be fit as follows:

$$\frac{\sigma}{10^{-21} \text{ cm}^2} = \begin{cases} 0.2186x^{-2} - 0.0344x^{-1} - 0.0054 & \text{if } x < 0 \\ 0.2367x^{-2} - 0.0187x^{-1} + 0.0004 & \text{if } x > 0 \end{cases} \quad (\text{A5})$$

Note that separate fits are given for the blue ($x < 0$) and red ($x > 0$) wings of H α since the cross section, although approximately Lorentzian, is not exactly symmetric, being stronger on the blue side (by about 10% for $x = \pm 1$).

The fraction of all $1s \rightarrow 3p$ excitations that result in Raman scattering to an optical photon is given by the branching ratio, $f_{\text{H}\alpha}$, with the remaining fraction, $1 - f_{\text{H}\alpha}$, resulting in elastic Rayleigh scattering in which the photon remains in the FUV domain. The results for $f_{\text{H}\alpha}$ are also shown in Figure 1 of Chang et al. (2015) and can be fit as follows in the range $|x| < 5$:

$$f_{\text{H}\alpha} = 0.2238 + 0.0363x + 0.0024x^2. \quad (\text{A6})$$

The relative accuracy of all these fits is better than 1% within

the stated range (corresponding to $\sigma \approx 10^{-22} \text{ cm}^2$ to 10^{-21} cm^2), which is perfectly adequate for the purposes of this paper. Note that the branching ratio increases with x , which means that the product $\sigma f_{\text{H}\alpha}$ is stronger on the red side of H α .

This paper has been typeset from a $\text{\TeX}/\text{\LaTeX}$ file prepared by the author.